**Universität Zürich** UZH

# Determination of the Invariant Mass Distribution for $B^0_{(s)} \to \mu^+ \mu^-$ at the LHCb Experiment

Master Thesis

of

Christian Elsasser

Mathematisch-naturwissenschaftliche Fakultät

der

Universität Zürich

Prof. Dr. U. Straumann
Dr. O. Steinkamp

Zürich
2011

Contact:
Christian Elsasser
Physics Institute, University of Zurich
Winterthurerstrasse 190
CH-8057 Zürich
elsasser@cern.ch
che@physik.uzh.ch

# Abstract

The branching fraction measurement of $B_s^0 \to \mu^+ \mu^-$ and $B^0 \to \mu^+ \mu^-$ is one of the key analysis for the LHC$b$ experiment. These branching fractions are predicted to be very small in the Standard Model and are highly sensitive to effects beyond the Standard Model. Therefore these decays can be used to detect indirectly New Physics.

LHC$b$ has published this year a result based on 2010 data. No signal was observed and an upper limit for the branching fractions has been set.

One of the corner stones in this analysis at LHC$b$ is the determination of the invariant mass distribution of the two muons for signal and background. The parameters of the signal distribution must be estimated from decays similar to $B_{(s)}^0 \to \mu^+ \mu^-$ such as $B_{(s)}^0 \to (\pi^+/K^+)(\pi^-/K^-)$ or $\psi(nS)/\Upsilon(nS) \to \mu^+\mu^-$ as no signal for $B_{(s)}^0 \to \mu^+\mu^-$ has been observed. A special focus in the determination of the parameters lies in the estimation of the systematic errors.

This thesis provides the determination of the invariant dimuon mass distribution and its statistical and systematic errors based on the 2010 data with different methods which have led to compatible results.

# Acknowledgement

Before starting with my thesis I would like to take the opportunity to thank a range of people who have enabled this thesis and supported me during the project.

First of all I thank Prof. Dr. Ulrich Straumann for giving me the chance to write my master thesis in the Zurich LHC*b* group. For the many fruitful discussions and his great support during my work I thank my advisor, Olaf Steinkamp.

Also a large contribution to the success of my work belongs to Diego Martinez Santos and Johannes Albrecht of the CERN LHC*b* group.

For the many interesting discussions and talks as well as their help in various areas of the analysis I am very grateful to various members of the Zurich LHC*b* group: Jonny Anderson, Roland Bernet, Angela Büchler, Albert Bursche, Nicola Chiapolini, Michel Decian, Katharina Müller, Christophe Salzmann, Nico Serra, Jeroen van Tillburg and Mark Tobin.

Further I would like to mention the people of CTA in our office, Arno Gadola, Roman Gredig and Ben Huber. It has been a great pleasure to share the office with you and I thank you for the great atmosphere.

Zurich, August 2011

Christian Elsasser

# Contents

# List of Figures

# List of Tables

# Introduction

The Large Hadron Collider (LHC) and its experiments have been running since spring 2010 at a center of mass energy of $\sqrt{s} = 7\,\text{TeV}$. The goal of this particle accelerator is, on one hand, the discovery of the last missing particle in the Standard Model (SM) of particle physics, the Higgs boson responsible for the other particles' masses. On the other hand the experiments are looking for signs of New Physics (NP) beyond the Standard Model. The LHC$b$ experiment is searching for such phenomena in the sector of Heavy Flavor particles, Hadrons containing charm and beauty quarks. Channels well-suited for such searches are the rare decays $B^0_{(s)} \rightarrow \mu^+\mu^-$ where $B^0_{(s)}$ means the $B^0$ or the $B^0_s$ meson. Many New Physics models can be tested by measuring the branching fractions of these decays. The present thesis provides methods to estimate the invariant mass distribution of the $B^0_{(s)}$ mesons decaying into two muons which forms an important input to this search.

Chapter 1 briefly describes the Standard Model of particle physics. Chapter 2 explains the LHC$b$ experiment and its detectors while Chapter 3 gives an overview on the impact of the branching fractions of $B^0_{(s)} \rightarrow \mu^+\mu^-$ in the Standard Model and beyond. Chapters 4 to 7 are devoted to the determination of the different parameters describing the invariant mass distribution.

The thesis is closed by a summary describing all parameters of the invariant mass distribution and its statistical and systematic errors in Chapter 8.

14

# 1 The Standard Model of Particle Physics

The Standard Model (SM) of particle physics describes the elementary particles, the smallest constituents of matter, and their interactions. The predictions derived from this model are in good agreement with experimental results.

## 1.1 Particle Spectrum and Interactions

The elementary particles in the SM can be split into two groups: fermions (half-integral spin) and bosons (integral spin). While the fermions, quarks and leptons, form the composite particles, the bosons are the carriers of the fundamental forces (cf. Tab. 1.1 and 1.2).

While interactions involving a photon, gluon or $Z^0$ boson do not change the flavor of the participating quarks, interactions with $W^\pm$ do this. There are not only flavor changes within the families (e.g. $d \to W^- u$), but also across families (e.g. $b \to W^- u$). The amplitude of such an interaction $i \to W j$ is proportional to the corresponding element $V_{ij}$ of the CKM matrix.

$$|V_{\mathrm{CKM}}| = \begin{pmatrix} |V_{ud}| & |V_{us}| & |V_{ub}| \\ |V_{cd}| & |V_{cs}| & |V_{cb}| \\ |V_{td}| & |V_{ts}| & |V_{tb}| \end{pmatrix} = \begin{pmatrix} 0.974 & 0.225 & 0.003 \\ 0.225 & 0.973 & 0.041 \\ 0.009 & 0.040 & 0.999 \end{pmatrix} \text{ [25]} \qquad (1.1)$$

Processes involving transitions across families are suppressed due to the dominance of the diagonal matrix elements (Cabbibo suppression), most strongly those involving quarks of the third family.

**Table 1.1:** Summary of fermions in the Standard Model

| Quantity | 1$^{st}$ family | 2$^{nd}$ family | 3$^{rd}$ family |
|---|---|---|---|
| | **Quarks** | | |
| | up ($u$) | charm ($c$) | top ($t$) |
| $q$ | 2/3 | 2/3 | 2/3 |
| $m$ | $=$ 2-3.5 MeV/c$^2$ | $=$ 1.27 GeV/c$^2$ | $=$ 172 GeV/c$^2$ |
| anti-particle[a)] | $\bar{u}$ | $\bar{c}$ | $\bar{t}$ |
| | down ($d$) | strange ($s$) | beauty ($b$) |
| $q$ | -1/3 | -1/3 | -1/ |
| $m$ | $=$ 4-5.5 MeV/c$^2$ | $=$ 101 MeV/c$^2$ | $=$ 4.67 GeV/c$^2$ |
| anti-particle[a)] | $\bar{d}$ | $\bar{s}$ | $\bar{b}$ |
| | **Leptons** | | |
| | electron ($e^-$) | muon ($\mu^-$) | tau ($\tau^-$) |
| $q$ | -1 | -1 | -1 |
| $m$ | $=$ 511 keV/c$^2$ | $=$ 105 MeV/c$^2$ | $=$ 1.78 GeV/c$^2$ |
| anti-particle[a)] | $e^+$ | $\mu^+$ | $\tau^+$ |
| | electron-neutrino ($\nu_e$) | muon-neutrino ($\nu_\mu$) | tau-neutrino ($\nu_\tau$) |
| $q$ | 0 | 0 | 0 |
| $m$ | $<$ 2 eV/c$^2$ 95% C.L. | $<$ 17 keV/c$^2$ 95% C.L. | $<$ 1.23 MeV/c$^2$ 95% C.L. |
| anti-particle[a)] | $\bar{\nu}_e$ | $\bar{\nu}_\mu$ | $\bar{\nu}_\tau$ |

[a)] Anti-particles have beside opposite charge-like quantum numbers the same qualities as the particles.

**Table 1.2:** Summary of interactions and bosons in the Standard Model

| Interaction | Electromagnetic | Weak force | Strong force |
|---|---|---|---|
| Gauge bosons | photon ($\gamma$) | $W^\pm$, $Z^0$ bosons | gluons ($g$; 8 pieces) |
| $m_{boson}$ | $=$ 0 eV/c$^2$ | $=$ 80.4 GeV/c$^2$($W^\pm$) $=$ 91.2 GeV/c$^2$($Z^0$) | $=$ 0 eV/c$^2$ |
| $q_{boson}$ | 0 | $\pm 1$ ($W^\pm$) 0 ($Z^0$) | 0 |
| acting on | all charged particles | all left-handed fermions and $W^\pm$, $Z^0$ | quarks and gluons |

[1] The Higgs boson postulated to explain the masses of all the other particles has spin 0 and interacts with all particles having masses.

# 1.2 *B* mesons and $c\bar{c}$-/$b\bar{b}$-mesons

The composite particles which are studied in this thesis are pseudoscalar (i.e. spin $J = 0$, but odd parity) *B* mesons as well as $c\bar{c}$- and $b\bar{b}$-mesons, also called Charmonia and Bottomia. These particles are listed in Tab. 1.3 with their relevant properties.

**Table 1.3:** Summary of *B* mesons as well as Charmonia and Bottomia states [25]

| Particle | Quark state | Mass $m$ $[\text{MeV/c}^2]$ | lifetime $\tau$ [ps] [a] |
|---|---|---|---|
| *B* **mesons** | | | |
| $B^0/\overline{B}^0$ | $|\bar{b}d\rangle/|b\bar{d}\rangle$ | 5279.5 | 1.52 |
| $B^+/B^-$ | $|\bar{b}u\rangle/|b\bar{u}\rangle$ | 5279.2 | 1.64 |
| $B_s^0/\overline{B}_s^0$ | $|\bar{b}s\rangle/|b\bar{s}\rangle$ | 5366.3 | 1.47 |
| $B_c^+/B_c^-$ | $|\bar{b}c\rangle/|b\bar{c}\rangle$ | 6277.0 | 0.45 |
| $c\bar{c}$-**mesons** | | | |
| $J/\psi(1S)$ | $|c\bar{c}\rangle$ | 3096.9 | $7.1 \cdot 10^{-9}$ |
| $\psi(2S)$ | $|c\bar{c}\rangle$ | 3686.0 | $2.1 \cdot 10^{-9}$ |
| $b\bar{b}$-**mesons** | | | |
| $\Upsilon(1S)$ | $|b\bar{b}\rangle$ | 9460.3 | $1.2 \cdot 10^{-8}$ |
| $\Upsilon(2S)$ | $|b\bar{b}\rangle$ | 10023.3 | $2.1 \cdot 10^{-8}$ |
| $\Upsilon(3S)$ | $|b\bar{b}\rangle$ | 10355.2 | $3.2 \cdot 10^{-8}$ |

[a] The lifetimes of the $c\bar{c}$- and $b\bar{b}$-mesons are taken as $\tau = \hbar/\Gamma$ from the measured decay width.

The $c\bar{c}$- and $b\bar{b}$-mesons decay mainly in processes involving the strong or electromagnetic interaction, leading to small lifetimes. There are several of these mesons which differ in mass due to different radial excitations, quark spin and angular momentum configurations. $J/\psi(1S)$ and $\psi(2S)$ as well as $\Upsilon(1S)$, $\Upsilon(2S)$ and $\Upsilon(3S)$ are all mesons with a total spin $J = 1$ and differ in the radial excitation.

The *B* mesons on the other hand offer due to their large masses, and as they only can decay through the weak force, many decay channels, which are good candidates to search for signs of physics beyond the Standard Model.

As the *b* quark can not decay within its family, *B* mesons have to decay Cabbibo suppressed leading to relatively long lifetimes of about $10^{-12}$ s which can be in the experiment taken as advantage to identify these mesons through their displaced decay vertices.

# 2 The LHCb experiment

## 2.1 The LHCb detector

The LHC*b* experiment is one of the four large experiments at the LHC[1]. Its main goals are the studies of $\mathcal{CP}$ violating processes in *B* physics as well as rare decays of *B* hadrons.

The LHC*b* detector is designed as a single-arm forward spectrometer with an acceptance in terms of pseudorapidity[2] of $\eta = 1.9 - 5.3$. The layout of the detector takes into account the enhanced production of *b* quarks under low angles with respect to the beam at Hadron colliders. The detector set-up is shown in Fig. 2.1.

**Tracking System**   The apparatus includes a tracking system formed by the Vertex Locator (VELO), the Tracker Turicensis (TT) – both built as micro-strip silicon detectors and located upstream of the dipole magnet – as well as the tracking stations (T1, T2, T3) downstream of the magnet. The latter are formed by the Inner Tracker (IT) around the beam pipe, which is also a micro-strip silicon detector, and by the Outer Tracker (OT) in the region farther away from the beam, which is based on straw tubes. The achieved relative momentum resolution is $\sigma_p/p = 0.3\%$ for $p = 1$ GeV/c and $\sigma_p/p = 0.45\%$ for $p = 100$ GeV/c [19].

**Hadronic Particle Identification**   There are two Ring Imaging Cherenkov Detectors (RICH) for particle identification, one for low momentum particles (2-60 GeV/c), located upstream of the magnet and running with Aerogel and $C_4F_{10}$ as radiators and one for high momentum particles (16-100 GeV/c) located downstream of the magnet and using $CF_4$ [23].

---

[1]The others are CMS (Compact Muon Solenoid) and ATLAS (A Toroidal LHC ApparatuS), both designed as multipurpose experiments and dedicated to Heavy Flavor physics as well as Higgs and New Physics searches, and ALICE (A Large Ion Collider Experiment), designed for heavy ion collisions and investigating e.g. quark-gluon plasma.

[2]The pseudorapidity is defined as $\eta = -\log(\tan(\theta/2))$ with $\theta$ as the angle between the momentum of the particle and the beam line, measured in the lab frame.
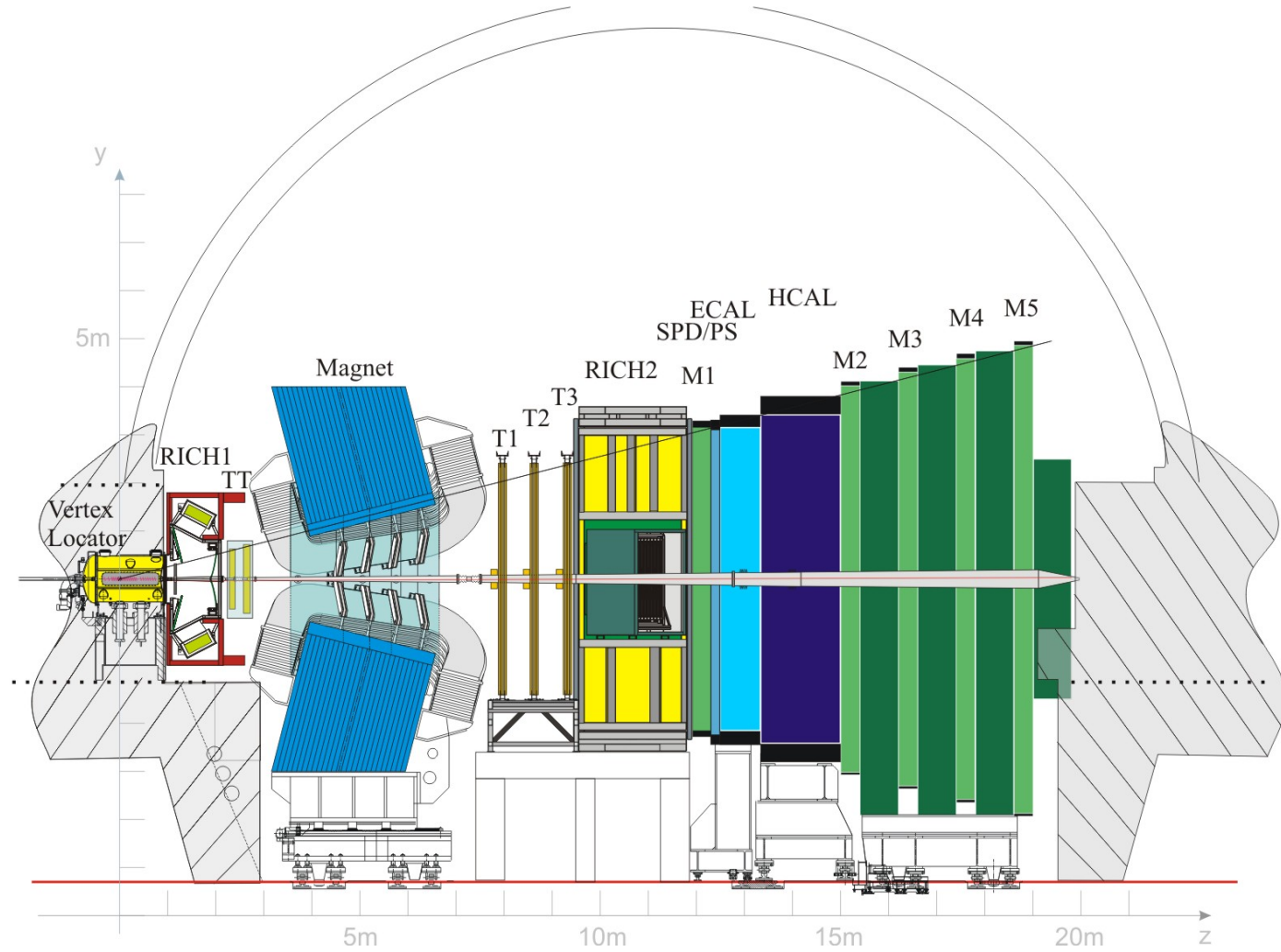
**Figure 2.1:** Side view of LHC*b* (VELO: VErtex LOcator, RICH: Ring Imaging CHerenkov detector, TT: Tracker Turicensis, T1/2/3: Tracking stations, SPD/PS: Scintillating Pad Detector/PreShower, ECAL: Electromagnetic CALorimeter, HCAL: Hadronic CALorimeter, M1-5: Muon detectors) [19]

**Calorimetry**   LHCb includes an Electromagnetic Calorimeter (ECAL) and a Hadronic Calorimeter (HCAL). The former is a sampling lead-scintillator device while the latter is made as a sampling detector consisting of iron as absorber and scintillating tiles as active part. In front of the ECAL there are a Scintillating Pad Detector (SPD) and a Preshower (PS) used to reject background of soft neutral and charged pions from the underlying event.

**Muon system**   The muon detectors (M1 - M5) are based on MWPC (Multiwire proportional chambers) and use in addition triple-GEM (Gaseous Electron Multiplier) in the area around the beam pipe to achieve a higher granularity and to take the faster aging of the detector in this region into account.

The calorimeters and the muon system are mainly dedicated to offline particle identification and trigger tasks [8].

**Trigger and data selection**   The LHCb trigger system is built up by three levels: The lowest level (L0-trigger) is implemented in hard ware and selects events with large transverse momenta in the muon system or large transverse energy in the calorimeters. This level reduces the event rate from the 40 MHz collision rate of LHC to about 1 MHz. The second level (HLT1-trigger) performs a partial reconstruction of the events and reduces based on lifetime and impact parameter information the rate by an additional factor of about 30.
Finally the third level (HLT2-trigger) uses the information of the fully reconstructed events to reduce the rate to 2 kHz. The events passing the HLT2-trigger are then written to tape and classified according to their topology in different so-called streams (e.g. events including hard photons, two muons, $b$ hadrons, etc.) and even finer in stripping lines. A stripping line corresponds to a coarse selection of events which will be used in a certain analysis (e.g. events most probable including a decay $J/\psi(1S) \rightarrow \mu^+\mu^-$).

## 2.2 The 2010 Data Taking

The LHC*b* experiment has collected about $37\,\mathrm{pb}^{-1}$ of integrated luminosity in the 2010 run (cf. Fig. 2.2). Using this data, the $b\bar{b}$-cross section at $\sqrt{s} = 7\,\mathrm{TeV}$ in the acceptance of the detector has been measured to be $\sigma(pp \rightarrow b\bar{b}X) = (75.3 \pm 5.4(\mathrm{stat.}) \pm 13.0(\mathrm{syst.}))\,\mu\mathrm{b}$. Extrapolating to the full phase space, a total cross section of $\sigma(pp \rightarrow b\bar{b}X) = (284 \pm 20(\mathrm{stat.}) \pm 49(\mathrm{syst.}))\,\mu\mathrm{b}$ is obtained [3].
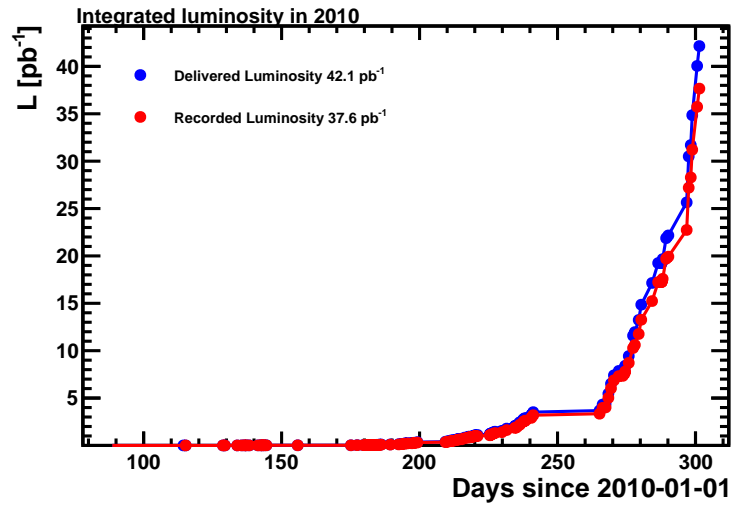


**Figure 2.2:** Delivered and collected integrated luminosity in 2010 for LHC*b* as a function of time.

# 3 Theory of $B^0_{(s)} \to \mu^+\mu^-$ and Analysis Strategy for LHCb

## 3.1 Relevance of $B^0_{(s)} \to \mu^+\mu^-$

### 3.1.1 $B^0_{(s)} \to \mu^+\mu^-$ in the Standard Model

In the Standard Model the decay $B^0_{(s)} \to \mu^+\mu^-$ is only allowed by Flavor-changing Neutral Currents (FCNC). As shown in the Feynman diagrams (cf. Fig. 3.1 and 3.2) the decay is heavily Cabbibo suppressed. It is further suppressed by helicity. The branching fractions predicted in the Standard Model are:

$$\mathcal{B}(B^0_s \to \mu^+\mu^-) = (3.2 \pm 0.2) \cdot 10^{-9} \text{ [14]}$$
$$\mathcal{B}(B^0 \to \mu^+\mu^-) = (1.0 \pm 0.1) \cdot 10^{-10} \text{ [14]}$$
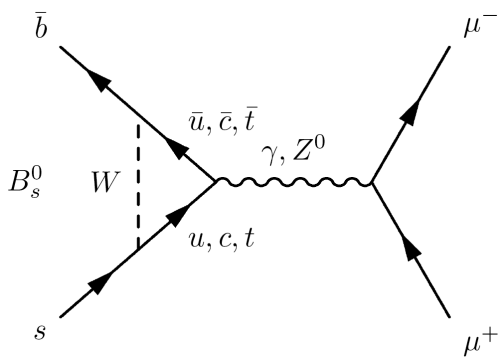


**Figure 3.1:** A Penguin diagram of $B^0_s \to \mu^+\mu^-$ in the Standard Model. The diagram is heavily Cabbibo suppressed due to the involved non-diagonal CKM-matrix elements at vertices involving the $W$ boson.
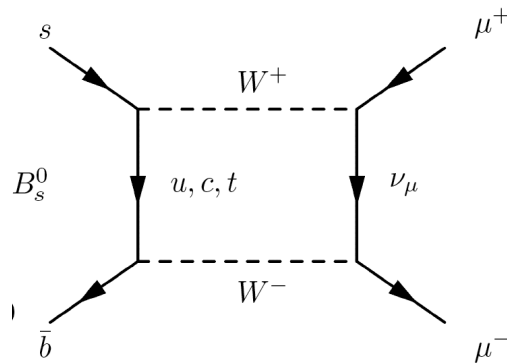
**Figure 3.2:** A Box diagram of $B^0_s \to \mu^+\mu^-$ in the Standard Model. As in the left diagram the diagram is Cabibbo suppressed.

With this low SM branching fractions, the decays are very sensitive to New Physics (NP) as their contributions to the decays might be of the same order of magnitude as the SM contribution.

The decays have so far not been observed. The lowest upper bounds for the branching fractions have been set by the two Tevatron experiments CDF and DØ[1]:

$$
\begin{aligned}
\mathcal{B}(B^0_s \to \mu^+ \mu^-) \quad &< 4.3 \cdot 10^{-8} \quad \text{at 95\% C.L. (CDF) [4]} \\
\mathcal{B}(B^0_s \to \mu^+ \mu^-) \quad &< 5.1 \cdot 10^{-8} \quad \text{at 95\% C.L. (DØ) [6]}
\end{aligned}
$$

$$
\mathcal{B}(B^0 \to \mu^+ \mu^-) \quad < 7.6 \cdot 10^{-9} \quad \text{at 95\% C.L. (CDF) [4]}
$$

## 3.1.2 $B^0_{(s)} \to \mu^+ \mu^-$ in New Physics Models

In many NP models a significant enhancement of the branching fractions for the decays is possible. In the following we briefly discuss a few of these models:

**Two Higgs Doublets Model**   So far the particles predicted by the Higgs mechanism, i.e. the Higgs bosons, have not been found. In principle different actual implementations of the mechanism are possible, which can differ in the number of involved Higgs bosons. Besides the simplest possibility in the SM, a single doublet of complex Higgs fields, there are possibilities – within but also beyond the SM, e.g. the Minimal Supersymmetric Standard Model (MSSM) – involving two doublets of complex Higgs fields. These two doublets would lead to a spectrum of five Higgs bosons: two charged, two neutral scalar ($\mathcal{CP}$-even) and one neutral pseudo-scalar ($\mathcal{CP}$-odd). As shown in Fig.

---

[1]Since the EPS 2011 conference (July 2011, Grenoble) there are now lowest upper bounds on the branching frations:

$$
\begin{aligned}
\mathcal{B}(B^0_s \to \mu^+ \mu^-) \quad &< 1.5 \cdot 10^{-8} \quad \text{at 95\% C.L. (LHC}b\text{) [1]} \\
\mathcal{B}(B^0_s \to \mu^+ \mu^-) \quad &< 1.9 \cdot 10^{-8} \quad \text{at 95\% C.L. (CMS) [16]}
\end{aligned}
$$

$$
\begin{aligned}
\mathcal{B}(B^0 \to \mu^+ \mu^-) \quad &< 5.2 \cdot 10^{-9} \quad \text{at 95\% C.L. (LHC}b\text{) [1]} \\
\mathcal{B}(B^0 \to \mu^+ \mu^-) \quad &< 4.6 \cdot 10^{-9} \quad \text{at 95\% C.L. (CMS) [16]}
\end{aligned}
$$

In addition there is a first branching fraction measurement by CDF of $\mathcal{B}(B^0_s \to \mu^+ \mu^-) = (1.8^{+1.1}_{-0.9}) \cdot 10^{-8}$ at 95% C.L. which could not be confirmed by LHC$b$ or CMS. The 95% confidence limit on $\mathcal{B}(B^0 \to \mu^+ \mu^-)$ by CDF is $6.0 \cdot 10^{-9}$[4].

3.3 those particles could contribute to the decay $B^0_{(s)} \to \mu^+ \mu^-$ and lead to a branching fraction proportional to fundamental parameters of the model

$$\mathcal{B}(B^0_{(s)} \to \mu^+ \mu^-) \propto \tan^4 \beta \cdot \left( \frac{\log m}{m-1} \right)^2, \text{ with } m = \frac{m^2_{H^\pm}}{m^2_t}, \qquad (3.1)$$

where $m_{H^\pm}$ is the mass of the charged Higgs bosons and $\tan \beta$ the ratio of the vacuum expectation values (VEV) of the two Higgs doublets [10, 13].
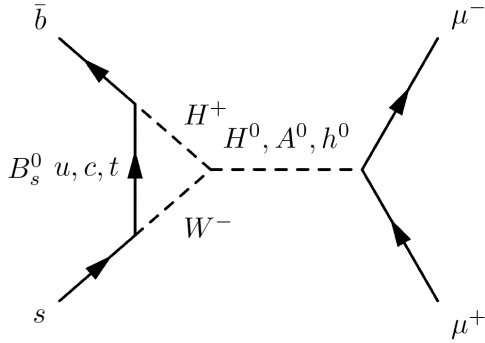


**Figure 3.3:** Feynman diagram for $B^0_s \to \mu^+ \mu^-$ in the Two Higgs Doublets Model. The diagram involves a charged Higgs boson as well as a neutral $\mathcal{CP}$-even ($H^0$,$h^0$) or $\mathcal{CP}$-odd ($A^0$) Higgs boson.
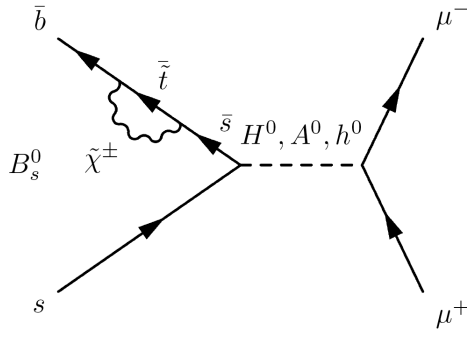
**Figure 3.4:** Feynman diagram for $B^0_s \to \mu^+ \mu^-$ in the Minimal Supersymmetric Standard Model. The diagram involves a chargino ($\tilde{\chi}^\pm$) as well as an anti-stop-quark $\bar{\tilde{t}}$ as supersymmetric particles and a neutral $\mathcal{CP}$-even ($H^0$,$h^0$) or $\mathcal{CP}$-odd ($A^0$) Higgs boson.

$Z'$ **Models**  A large number of models (e.g. Grand Unified Theories, theories involving extra dimensions, Supersymmetric String Theory) predict the existence of a vector boson heavier than the $Z^0$, called $Z'$. Such a boson could contribute to the decay $B^0_{(s)} \to \mu^+ \mu^-$ as replacement of $\gamma^*/Z^0$ in the SM diagrams (cf. Fig. 3.1) and lead to an enhanced branching fraction of $\mathcal{B} = \mathcal{O}(10^{-8})$ [24].

**Minimal Supersymmetric Standard Models**  The enhancement of the particle spectrum in supersymmetric models, i.e. the postulation of bosonic (fermionic) supersymmetric partners to all fermions (bosons) in the Standard Model, gives rise to many additional contributions to $B^0_{(s)} \to \mu^+ \mu^-$ (cf. Fig. 3.4).
The predicted branching fraction depends on the actual configuration of the model,

e.g. $\mathcal{R}$-parity[2] violating MSSM, maximally $\mathcal{CP}$-violating MSSM, etc. For example the MSSM with Non-Universal Higgs Masses (NUHM) – the masses of the two $\mathcal{CP}$-even Higgs bosons can be different – predicts a branching fraction of

$$\mathcal{B}(B^0_{(s)} \to \mu^+ \mu^-) \propto \frac{\tan^6 \beta}{M^4_{A^0}}, \tag{3.2}$$

where $M_{A^0}$ is the mass of the pseudo-scalar Higgs boson [10].

Besides the decays also test other theories such as Technicolor and Minimal Supergravity (mSUGRA) [12].
A precise measurement of their branching fractions allows to check the validity of a wide range of models, to restrict their allowed parameter spaces and thereby to indirectly search for signs of New Physics.

## 3.2 Analyisis Strategy for LHCb

The measurement of the branching fractions of $B^0_{(s)} \to \mu^+ \mu^-$ at LHC$b$ can be summarized by the following analysis steps:

1. The data set is reduced to a manageable size by applying loose selection cuts. The signal region ($B^0_{(s)} \pm 60\,\mathrm{MeV/c^2}$) is blinded.

2. A topological multi-variate classifier, the Geometrical Likelihood (GL)[3], is used to separate signal and background (mostly from $b\bar{b} \to \mu^+ \mu^- X$) events. Every event has a GL value between 0 and 1 indicating how likely an event is a signal (1) or a background (0) event. In addition the invariant mass of the two muons is used to discriminate signal and background. Signal events have an invariant mass of the muons close to the mass of $B^0_{(s)}$ according to the expected invariant mass distribution for $B^0_{(s)} \to \mu^+ \mu^-$.

---

[2] $\mathcal{R}$-parity is a proposed concept in Supersymmetry of a multiplicative conserved number $R$ where every SM particle has an $R$-value of $R = 1$ while the Supersymmetric particles have $R = -1$. Therefore the lightest supersymmetric particle (LSP) could not decay into $n$ SM particles ($R_{\mathrm{LSP}} = -1 \neq 1 = R^n_{\mathrm{SM}}$) and would be as a stable particle a candidate for dark matter.

[3] The GL is built from kinematical and topological variables (distance of closest approach between the two muons, isolation of the muons and $\chi^2$ of the impact parameter of the muons with respect to the primary vertex; transverse momentum, lifetime and impact parameter of the $B$ meson) of a two-body decay. For signal events the spectrum should be flat between 0 and 1, while it is strongly peaking at 0 for background events. More details in Ref. [2].

3. The number of signal-like events for a given value of $\mathcal{B}(B^0_{(s)} \to \mu^+\mu^-)$ is extracted from the observed number of detected signal events in channels with a similar characteristic ($B^+ \to J/\psi(\mu^+\mu^-)K^+$, $B^0 \to K^+\pi^-$ and $B^0_s \to J/\psi(\mu^+\mu^-)\phi(K^+K^-)$) and with well-known branching fractions.

4. The upper limit on $\mathcal{B}(B^0_{(s)} \to \mu^+\mu^-)$ is then extracted by comparing the number of detected events within a certain range of the GL and the invariant dimuon mass with the expected number of events in this range under the background only hypothesis and under the hypothesis of background and signal with a certain $\mathcal{B}(B^0_{(s)} \to \mu^+\mu^-)$. This method is called binned CL$_s$-method [27, 21].

The signal invariant dimuon mass distribution used to separate signal and background events as explained under point 2 is described by a Crystal Ball function [18]:

$$
f(x; n, \alpha, \mu, \sigma) \;=\; N \cdot
\begin{cases}
\exp\left(-\dfrac{(x-\mu)^2}{2\sigma^2}\right), & \text{if } \frac{x-\mu}{\sigma} > -\alpha, \\[2mm]
\left(\dfrac{n}{|\alpha|}\right)^n \cdot \exp\left(-\dfrac{|\alpha|^2}{2}\right) \cdot \left(\dfrac{n}{|\alpha|} - |\alpha| - \dfrac{x-\mu}{\sigma}\right)^{-n}, & \text{if } \frac{x-\mu}{\sigma} \leq -\alpha,
\end{cases}
\tag{3.3}
$$

where $\mu$ is the mean and $\sigma$ the width of the Gaussian, while $n$ is the exponent of the exponential tail and $\alpha$ the transition point at which the function changes from the exponential to the Gaussian regime. $N$ is the normalization factor of the PDF.

The following chapters describe the estimation of these four parameters: $\mu$ (Chapter 4), $\sigma$ (Chapters 5 and 6), $n$ and $\alpha$ (Chapter 7).

As there is obviously no possibility to extract these parameters from the signal channel itself, they must be either estimated from Monte Carlo simulation or from decays similar in topology with same initial or final states. These decays are for example $B^0 \to K^+\pi^-$ or $\Upsilon(1S) \to \mu^+\mu^-$. The latter approach has the advantage of relying as little as possible on Monte Carlo simulations. Chapter 8 finally combines the parameters to build the signal PDF.

# 4 $B^0$ and $B^0_s$ Masses

The first parameter of the Crystal Ball function (cf. (3.3)) to be considered is the mean of the Gaussian $\mu$. We can not simply use the nominal values of $m_{B^0}$ and $m_{B^0_s}$ as there might be a systematic bias in the reconstructed invariant mass, for example due to a not perfectly described dipole magnet field. Therefore other two-body decay modes of $B^0$ and $B^0_s$ are used for the determination.

## 4.1 Data Sample and Analysis Strategy

### 4.1.1 Data Sample and Selection

An inclusive $B^0_{(s)} \to h^+ h^-$ sample[1] is used, where $h^\pm$ can be a charged kaon or pion which are separated from each other using the particle identification from the RICH. The masses of $B^0$ and $B^0_s$ are extracted from fits to the invariant mass distribution of the two final state particles.

The used data is the full data set of $37\,\mathrm{pb}^{-1}$ in 2010 which forms also the base for all the following analyses. The following cuts are applied for the $B^0_{(s)} \to h^+ h^-$ sample to reduce background:

- For the final state particles $h^\pm$ we demand a good track fit of $\chi^2_\mathrm{track}/\mathrm{ndf} < 5$ and a clear separation from the primary vertex by $\chi^2_\mathrm{IP} > 25$, where IP is the impact parameter of the track to the primary vertex and $\chi^2_\mathrm{IP}$ is the square of the impact parameter divided by its error.

- For the $B^0_{(s)}$ we want to have a small distance of closest approach (DOCA) of the two associated tracks (DOCA $< 0.3\,\mathrm{mm}$), a good fit of the decay vertex by $\chi^2_\mathrm{SV} < 9$, a good pointing of the reconstructed $B^0_{(s)}$ momentum to the primary vertex by $\chi^2_\mathrm{IP} < 25$ and a clear separation of the primary and secondary vertex by VDS $> 15$, where VDS is the vertices distance significance (i.e. distance between

---

[1]If not explicit indicated, the charge conjugated decays are always meant to be included.

the two vertices divided by the error on their positions). Furthermore we impose a mass window of $\pm 600\,\mathrm{MeV/c^2}$ around the nominal mass of $B_s^0$.

On top of this selection, we enhance the signal fraction by demanding GL $> 0.1$.

## 4.1.2 Strategy and Fit Models

The basic strategy is to separate the different $B_{(s)}^0 \to h^+ h^-$ decay modes $B_{(s)}^0 \to \pi^+ \pi^-$, $B_{(s)}^0 \to K^+ \pi^-$, $B_{(s)}^0 \to \pi^+ K^-$ and $B_{(s)}^0 \to K^+ K^-$ by applying cuts on the particle identification (PID) of the reconstructed particles. This allows us to select the correct hypothesis of the final state particles (kaon or pion) and therefore assign their correct masses which are then used in the reconstruction of the invariant mass of the $B$ meson.

The significance of a particle hypothesis, i.e. that a particle is of type $i$ and not of type $j$, is represented by the DLL$_{i-j}$ (delta log-likelihood) value. The larger this value is the more likely the particle is of type $i$ than of type $j$. A value of zero means equal probabilities to be of type $i$ or $j$ (cf. Chapter 6).

We demand a DLL$_{K-\pi}$ value greater than 10 to identify a particle as a kaon and smaller than $-10$ to identify it as a pion. This gives samples with a purity above 98% and an overall efficiency of about 73%, so no bias in the reconstructed invariant mass due to misidentified particles has to be expected [26].

In addition there is the chance of misidentifying the proton from the decay modes $\Lambda_b^0 \to p\pi^- / K^-$ as a kaon or a pion leading to a contamination of the $B_{(s)}^0 \to h^+ h^-$ decay modes. To avoid this, we demand in addition a DLL$_{K-p}$ and DLL$_{\pi-p}$ value greater than zero.

**Table 4.1:** Branching fractions of $B_{(s)}^0 \to h^+ h^-$ [25]

| $hh$ | $\mathcal{B}(B^0 \to h^+ h^-)$ | $\mathcal{B}(B_s^0 \to h^+ h^-)$ |
|---|---|---|
| $\pi^+ \pi^-$ | $=(5.13\pm0.24)\cdot10^{-6}$ | $<1.2\cdot10^{-6}$ @ 90% C.L. |
| $\pi^+ K^-$ | $-$ a) | $=(4.9\pm1.0)\cdot10^{-6}$ |
| $K^+ \pi^-$ | $=(1.94\pm0.06)\cdot10^{-5}$ | $-$ a) |
| $K^+ K^-$ | $<4.1\cdot10^{-7}$ @ 90% C.L. | $=(3.3\pm0.9)\cdot10^{-5}$ |

a) No value or upper limit has yet been measured.

The branching fractions for the different decay modes are listed in Tab. 4.1. In the $\pi^+ \pi^-$ final state, we expect a signal only from $B^0$ decays, while in the $K^+ K^-$ final state we expect a signal only from $B_s^0$ decays.

In the $K^+ \pi^-$ ($\pi^+ K^-$) mode we expect a dominating signal from $B^0$ ($\overline{B}^0$) and a smaler one from $\overline{B}_s^0$ ($B_s^0$).

Therefore we use for the $\pi^+ \pi^-$ and $K^+ K^-$ distributions a double Crystal Ball function
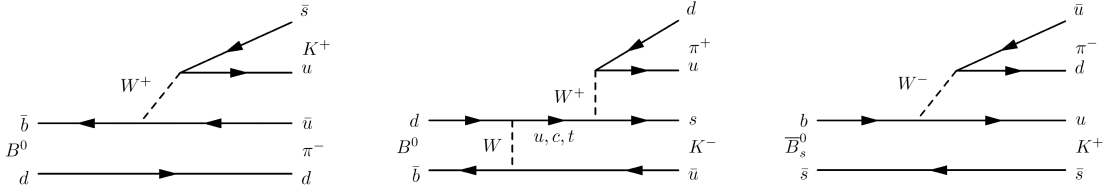
**Figure 4.1:** Leading order Feynman diagram of $B^0 \to K^+ \pi^-$ (l.), leading order Feynman diagram of $B^0 \to \pi^+ K^-$ surpressd by a factor $\alpha_W^2$ due to the additional $W$ boson (m.) and leading order Feynman diagram of $\overline{B}^0_s \to K^+ \pi^-$ (r.)

(4.1) to describe the invariant mass distribution for signal, while for $K^+ \pi^-$ and $\pi^+ K^-$ we use two double Crystal Ball functions

$$f(m; n, \alpha, \mu, \sigma) = N \cdot \begin{cases} \left(\frac{n_l}{|\alpha_l|}\right)^{n_l} \cdot \exp\left(-\frac{|\alpha_l|^2}{2}\right) \cdot \left(\frac{n_l}{|\alpha_l|} - |\alpha_l| - \frac{m-\mu}{\sigma}\right)^{-n_l}, & \text{if } \frac{x-\mu}{\sigma} \leq -\alpha_l, \\ \left(\frac{n_r}{|\alpha_r|}\right)^{n_r} \cdot \exp\left(-\frac{|\alpha_r|^2}{2}\right) \cdot \left(\frac{n_r}{|\alpha_r|} - |\alpha_r| - \frac{m-\mu}{\sigma}\right)^{-n_r}, & \text{if } \frac{x-\mu}{\sigma} \geq \alpha_r, \\ \exp\left(-\frac{(m-\mu)^2}{2\sigma^2}\right), & \text{else,} \end{cases}$$

(4.1)

where $N$ is the normalization factor, $n_{l,r}$ are the exponent of the left and right tails, $\alpha_{l,r}$ the turning points of the left and right tails respectively.

The left hand tail of the double Crystal Ball function takes final state radiation (FSR) and interaction with matter into account while the right hand tail describes non-gaussian detector effects. A relinquishment of the right hand tail (i.e. the use of a single Crystal Ball) could result in a bias of the mean as well as of the sigma of the Gaussian.
Contaminations from $\Lambda_b^0 \to p\pi^- / K^-$ are neglected due to the small branching ratios ($\mathcal{B}(\Lambda_b^0 \to p\pi^-) = (3.8 \pm 1.3) \cdot 10^{-6}$, $\mathcal{B}(\Lambda_b^0 \to pK^-) = (6.0 \pm 1.9) \cdot 10^{-6}$), the small $b$ hadronization fraction into $\Lambda_b^0$ (less than 8.5%) [25] and the fact that most of these events are eliminated by the applied PID cuts.
The invariant mass distribution of the combinatorial background is described by an exponential distribution. In addition there is a physical background contribution from $B \to hhh$ decays where one track is not correctly reconstructed and therefore fakes a two-body decay. Due to the missing track in the reconstruction of the invariant mass of the $B$ meson, this background appear at masses below the $B$ meson masses. To describe

this background, we use as distribution the phenomenological function [15]:

$$f(m;m_0,c_p,\sigma_p) = N \cdot m \left(1 - \frac{m^2}{m_0^2}\right) \Theta(m_0 - m) \exp(-c_p \cdot m) \otimes \frac{1}{\sqrt{2\pi}\sigma_p} \exp\left(-\frac{m^2}{2\sigma_p^2}\right),$$

$$(4.2)$$

where $N$ is the normalization factor and $\Theta$ the Heaviside thetafunction. The convolution acts on $m$.

## 4.2 Analysis and Results

### 4.2.1 Monte Carlo for $B^0_s \rightarrow \mu^+\mu^-$

In a first step we use an exclusive $B^0_s \rightarrow \mu^+\mu^-$ Monte Carlo sample[2] to extract the values of the parameters $n_l$, $\alpha_l$, $n_r$ and $\alpha_r$ of the double Crystal Ball function. In the fit of the invariant mass distribution of the $B^0_{(s)} \rightarrow h^+h^-$ from data we fix these parameters to the values extracted from the Monte Carlo sample as there are strong correlations among them and between them and the exponential parameter describing the combinatorial background.

Fig. 4.2 shows the reconstructed invariant mass distribution for the $B^0_s \rightarrow \mu^+\mu^-$ Monte Carlo sample together with the fitted double Crystal Ball and Tab. 4.2 displays the values of the parameters extracted from the Maximum Likelihood fit.

**Table 4.2:** Fit parameters of $B^0_s \rightarrow \mu^+\mu^-$ Monte Carlo

| Parameter | Value |
|---|---|
| $\alpha_l$ | 1.56±0.04 |
| $\alpha_r$ | -1.40±0.07 |
| $n_l$ | 1.43±0.08 |
| $n_r$ | 9.80±2.00 |
| $\mu$ | 5366.95±0.17 MeV/c$^2$ |
| $\sigma$ | 18.75±0.15 MeV/c$^2$ |

---

[2]All Monte Carlo samples used in this thesis were generated using the LHC*b* application GAUSS v39r0 based on LHCb v26r3, Pythia 6.418.2, PHOTOS 215.2, LHAPDF 5.3.1, HepMC 1.26 and GEANT4 v91r3.p03. The reconstruction used the LHC*b* applications BOOLE v21r9 and BRUNEL v37r8p5.
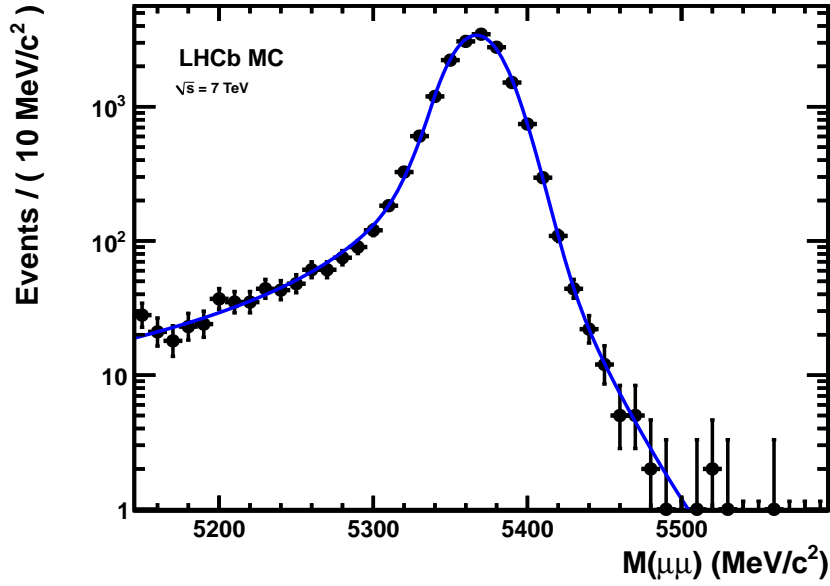
**Figure 4.2:** Invariant mass distribution of $B_s^0 \to \mu^+\mu^-$ Monte Carlo fitted with a double Crystal Ball function

## 4.2.2 Invariant Mass Distribution for $B_{(s)}^0 \to hh$

Fig. 4.3 to 4.6 show the invariant mass distributions for the different $B_{(s)}^0 \to h^+h^-$ decay modes together with the fit models described in Sec. 4.1.2[3]. The extracted values of the fit are displayed in Tab. 4.3.

**Table 4.3:** Values of $m_{B^0}$, $m_{B_s^0}$ and $f_{B^0}$ from the invariant mass fit of the $B_{(s)}^0 \to h^+h^-$ decay modes

| Decay mode | $m_{B^0}$ | $m_{B_s^0}$ | $f_{B^0}$ |
|---|---|---|---|
| $B_{(s)}^0 \to \pi^+\pi^-$ | $5276.0\pm2.5\,\mathrm{MeV/c^2}$ | — [a] | — [a] |
| $B_{(s)}^0 \to \pi^+K^-$ | $5275.1\pm1.3\,\mathrm{MeV/c^2}$ | $5363 \pm6\ \mathrm{MeV/c^2}$ [b] | $0.900\pm0.019$ |
| $B_{(s)}^0 \to K^+\pi^-$ | $5276.5\pm1.5\,\mathrm{MeV/c^2}$ | $5364 \pm9\ \mathrm{MeV/c^2}$ [b] | $0.955\pm0.024$ |
| $B_{(s)}^0 \to K^+K^-$ | — [a] | $5362.2\pm1.6\,\mathrm{MeV/c^2}$ | —[a] |

[a] No value extracted.
[b] Value will not further be considered.

For the $\pi^+K^-$ and $K^+\pi^-$ channels, $f_{B^0}$ is the fraction of the total number of signal

---

[3]The reconstruction of the all events in this thesis has been done with BRUNEL v37r8p4 with the Condition Database head-20101026 and the Detector Database head-20101026. The reconstructed data was then analyzed with the LHC*b* application DAVINCI v26r3p2.
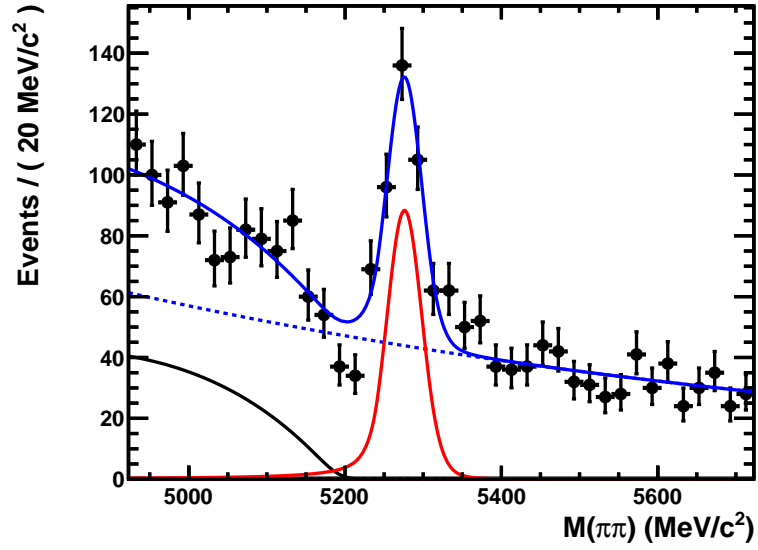
**Figure 4.3:** Invariant mass distribution for $\pi^+\pi^-$ from data. The blue solid (–) line is the full fit model while the blue dashed (- -) line shows the combinatorial background, the black solid line the physical background and the red solid line the $B^0/\overline{B}^0 \to \pi^+\pi^-$ signal.
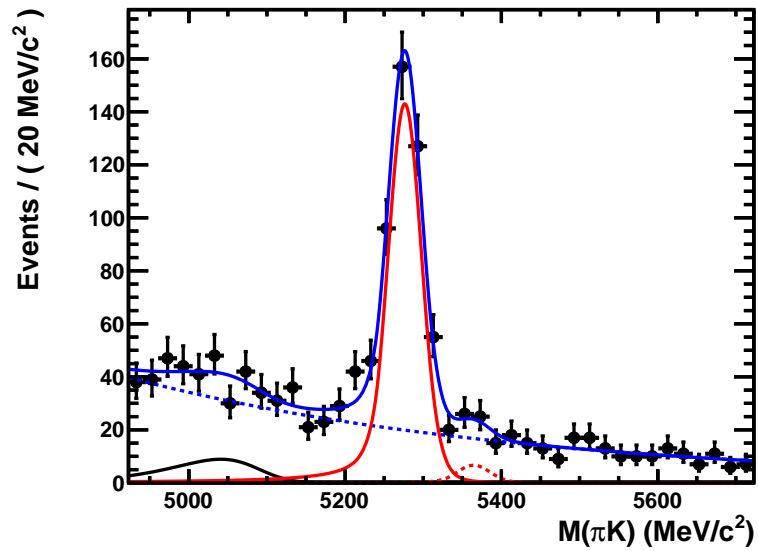


**Figure 4.4:** Invariant mass distribution for $K^+\pi^-$ from data. The blue solid (–) line is the full fit model while the blue dashed (- -) line shows the combinatorial background, the black solid line the physical background, the red solid line the $B^0 \to K^+\pi^-$ signal and the red dashed line the $\overline{B}_s^0 \to K^+\pi^-$ signal.
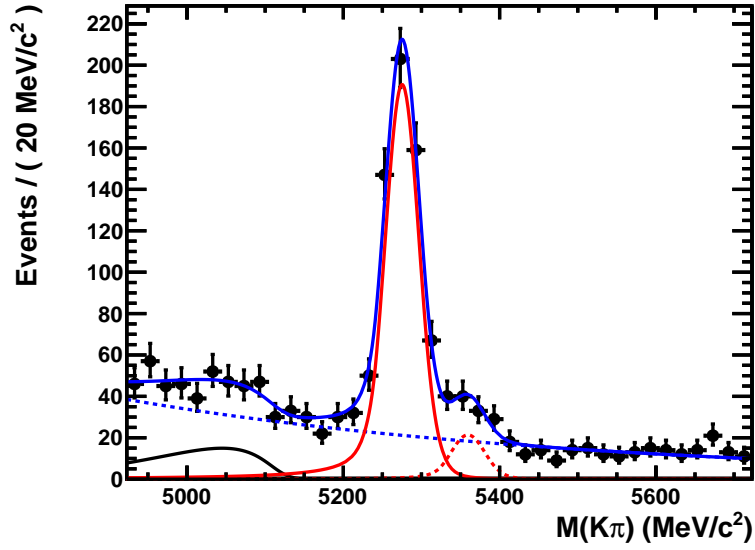
**Figure 4.5:** Invariant mass distribution for $\pi^+ K^-$ from data. The blue solid (–) line is the full fit model while the blue dashed (- -) line shows the combinatorial background, the black solid line the physical background, the red solid line the $\overline{B}^0 \to \pi^+ K^-$ signal and the red dashed line the $B_s^0 \to \pi^+ K^-$ signal.
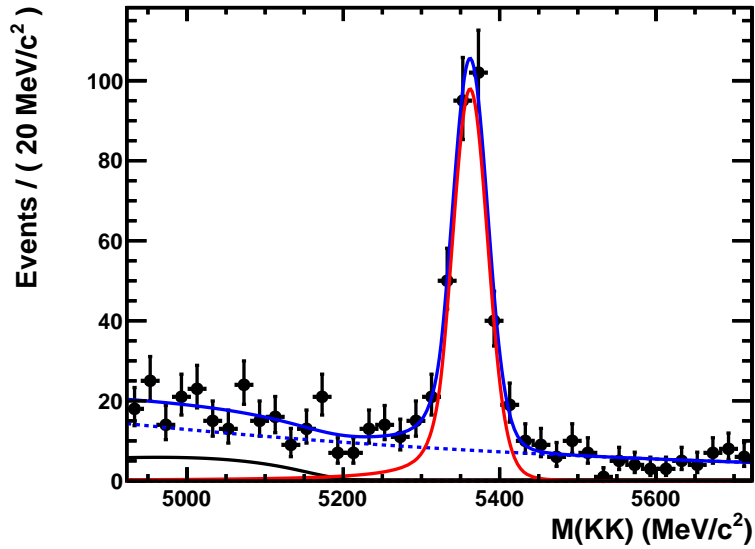


**Figure 4.6:** Invariant mass distribution for $K^+ K^-$ from data. The blue solid (–) line is the full fit model while the blue dashed (- -) line shows the combinatorial background, the black solid line the physical background and the red solid line the $B_s^0 / \overline{B}_s^0 \to K^+ K^-$ signal.

events associated to $B^0/\overline{B}^0$. The theoretical calculation of this value for $B_{(s)}^0 \rightarrow \pi^+K^-$ is shown in (4.3) while (4.4) shows the same value for $B_{(s)}^0 \rightarrow K^+\pi^-$.

$$f_{B^0} = \frac{(1-\alpha) \cdot \mathcal{B}(\overline{B}^0 \rightarrow \pi^+K^-)}{(1-\alpha) \cdot \mathcal{B}(\overline{B}^0 \rightarrow \pi^+K^-) + \frac{f_s}{f_d} \cdot 0.5 \cdot \mathcal{B}(B_s^0 \rightarrow \pi^+K^-)} \tag{4.3}$$

$$f_{B^0} = \frac{\alpha \cdot \mathcal{B}(B^0 \rightarrow K^+\pi^-)}{\alpha \cdot \mathcal{B}(B^0 \rightarrow K^+\pi^-) + \frac{f_s}{f_d} \cdot 0.5 \cdot \mathcal{B}(\overline{B}_s^0 \rightarrow K^+\pi^-)} \tag{4.4}$$

Here, $f_d/f_s$ is the ratio of the hadronization fractions of a $b$ quark to form a $B^0$ meson or a $B_s^0$ meson respectively. The current world average for this ratio is $3.71 \pm 0.41$ [11]. Furthermore, $\alpha$ is the relative fraction of $B^0$ mesons to the total number of produced $B^0$ and $\overline{B}^0$ mesons. It has the theoretical value of 0.6 at the LHC center of mass energy of $\sqrt{s} = 7\,\text{TeV}$ [9]. This production asymmetry bases on the flavor asymmetry of $pp$ colliders as there are only $d$ and $u$ valence quarks in the remnants of diffracted protons and not $\overline{d}$ and $\overline{u}$ valence quarks. Therefore it is more likely for a $\overline{b}$ quark to hadronize into a meson than for a $b$ quark which has an enhanced probability to form with the remnants a baryon. While in case of $B_s^0/\overline{B}_s^0$ mesons the situation should be symmetric (prefactor 0.5). The theoretical calculation leads to:

$B_{(s)}^0 \rightarrow \pi^+K^-$: $f_{B^0} = 0.922 \pm 0.020$

$B_{(s)}^0 \rightarrow K^+\pi^-$: $f_{B^0} = 0.946 \pm 0.010$,

where we used the branching fractions shown in Tab. 4.1. These values are in good agreement with the measured values displayed in Tab. 4.3, but we have not considered any error on $\alpha$ as well as any $\mathcal{CP}$ violation effect.

### 4.2.3 Systematics

The following sources of systematics have been taken into account for the determination of $\mu$, respectively $m_{B_{(s)}^0}$:

1. **Cut on the GL value:** The systematics due to the imposed cut on the GL value has been estimated by changing this cut value to GL $= \{0.05, 0.15\}$.

2. **Cut on the different DLL values:** The same procedure has been done for the DLL values, changing $\text{DLL}_{K-\pi}$ to $\{8, 12\}$ and $\overline{\text{DLL}}_{K/\pi-p}$ to $\{-2, 2\}$.

3. **Value of $f_{B^0}$:** To estimate effects due to the value of $f_{B^0}$ we fixed $f_{B^0}$ to the calculated theoretical value. As the theoretical and extracted values are in agreement,

the effect on $m_{B^0_{(s)}}$ has been below 0.1 MeV/c$^2$.

4. **Fit model:** The effect induced by the described Crystal Ball fit model has been estimated by changing to a Gaussian for the signal peaks. The effect on $\mu$ is a maximal shift of 0.2 MeV/c$^2$ and can therefore be neglected compared to the effects of the systematics due to the GL and DLL cuts.

These systematics as well as the values and the statistical errors are listed in Tab. 4.4. The combined systematical error is the square root of the quadratic sum of the single values as the correlations between the individual systematics are neglectable.

**Table 4.4:** Extracted values for $\mu$, statistical errors and systematic errors

| | $(B^0 \to \pi^+\pi^-)$ | $(B^0 \to \pi^+K^-)$ | $(B^0 \to K^+\pi^-)$ | $(B^0_s \to K^+K^-)$ |
|---|---|---|---|---|
| | all values in MeV/c$^2$ | | | |
| $\mu$ | 5276.0 | 5275.1 | 5276.5 | 5362.2 |
| **stat.** | 2.5 | 1.3 | 1.5 | 1.6 |
| **syst.** | | | | |
| GL | 2.0 | 1.0 | 1.8 | 1.0 |
| DLL$_{K-\pi}$ | 0.8 | 0.5 | 0.2 | 1.9 |
| DLL$_{K/\pi-p}$ | 0.1 | 0.2 | 0.4 | 1.1 |
| **combined** | 2.2 | 1.1 | 1.9 | 2.4 |

## 4.2.4 Results

In case of $m_{B^0}$ we combine the three results by taking the weighted average using $1/(\sigma^2_{\text{stat.}} + \sigma^2_{\text{syst.}})$ as weighting factors. The combined statistical error is defined by

$$\sigma_{\text{stat., comb.}} = \sqrt{\frac{1}{\sum 1/\sigma^2_{\text{stat.}}}}. \tag{4.5}$$

The combined systematical error is defined as the weighted average of the individual systematical errors using also $1/(\sigma^2_{\text{stat.}} + \sigma^2_{\text{syst.}})$ as weighting factors because the systematics of the different decay modes are correlated.

We obtain the following values for the parameter $\mu$ of the invariant mass distribution for $B^0_{(s)} \to \mu^+\mu^-$

$$B^0 \to \mu^+\mu^- : \quad \boxed{\mu = 5275.6 \pm 0.9 \,(\text{stat.}) \pm 1.5 \,(\text{syst.}) \,\text{MeV/c}^2} \tag{4.6}$$

$$B^0_s \to \mu^+\mu^- : \quad \boxed{\mu = 5362.2 \pm 1.6 \,(\text{stat.}) \pm 2.4 \,(\text{syst.}) \,\text{MeV/c}^2} \tag{4.7}$$

# 5 Invariant Mass Resolution from Interpolation of Charmonium and Bottomium Resonances

The first method discussed in this thesis to estimate the resolution $\sigma$ of (3.3) uses a linear interpolation between the measured resolutions for Charmonium and Bottomium resonances decaying into two muons. The basic idea behind this approach is that the invariant mass resolution as a function of the invariant mass can be predicted by using the Gluckstern Formula and relativistic kinematics. In Sec. 5.1 and 5.2 we are deriving this dependence from the Gluckstern Formula and making a cross-check with Drell-Yan[1] Monte Carlo.

## 5.1 The Gluckstern Formula

The Gluckstern Formula is a description of the relative measurement error on the momentum $\sigma_p/p$ for a charged particle measured by the bending of its trajectory in a homogeneous magnetic field [20, 22]. The formula predicts that $\sigma_p/p$ consists of a term linear in $p$, one proportional to $1/p$ and a constant term:

$$\frac{\sigma_p}{p} = \sqrt{(A \cdot p)^2 + \left(B \cdot \frac{1}{p}\right)^2 + C^2} \qquad (5.1)$$

The linear term represents the error due to the finite resolution of the tracking detectors, the second term the error due to multiple scattering and the constant term the error on the angle of the track with respect to the magnetic field lines.
But the Gluckstern Formula is based on many assumptions and simplifications that are only partially valid in real experiments: The magnetic field strength is assumed to be constant and the track measurements should be equidistant as well as their number

---

[1]Drell-Yan names the process $pp \to l^+l^-$ where $l^\pm$ is a charged lepton. In this thesis we are only looking at Drell-Yan processes with muons in the final state.

should be independent of the momentum. The numbers of average track hits in the different tracking detectors of LHC*b* as a function of the track momentum are displayed in Fig. 5.1 to show that the assumptions for the Gluckstern Formula are only partially valid.
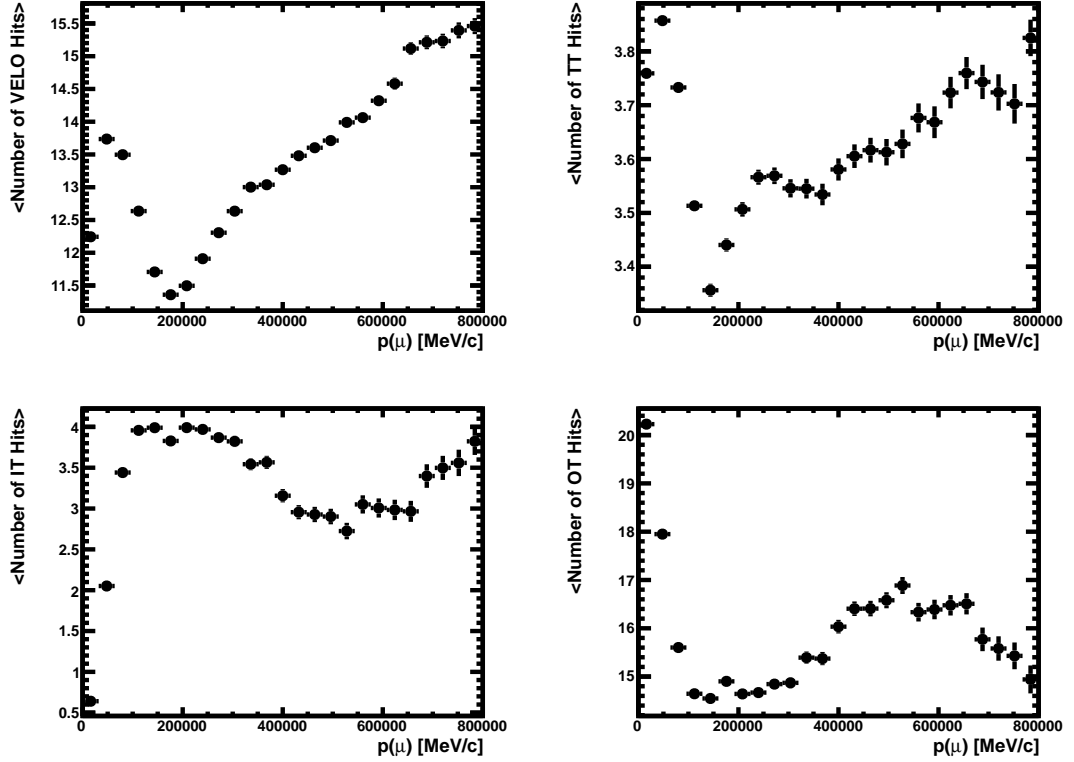


**Figure 5.1:** Average number of track hits in the different trackings detectors of LHC*b* as a function of the track momentum: Vertex Locator (t.l.), Tracker Turicensis (t.r.), Inner Tracker (b.l.) and Outer Tracker (b.r.) based on muons from Drell-Yan production. The vertical axes are zero-suppressed.

We check the validity of the Gluckstern Formula for muons by looking at Drell-Yan Monte Carlo samples with invariant dimuon masses between 2 and 22 GeV/c$^2$.

Fig. 5.2 shows the relative error on the momentum of the muons as a function of the momentum. The relative error is taken as the standard deviation of the distribution of the differences between the reconstructed and the true momentum divided by the true momentum. The figure shows that the data does not follow a linear behaviour in the region of highest momenta (i.e. above 100 GeV/c), but rather a power law. This deviation from the Gluckstern formula is a reflexion of the above mentioned assumptions and

simplifications. We quantify it by replacing the linear term in (5.1) by $A \cdot p^{\gamma}$

$$\frac{\sigma_p}{p} = \sqrt{(A \cdot p^{\gamma})^2 + \left(B \cdot \frac{1}{p}\right)^2 + C^2} \qquad (5.2)$$

leading to $\gamma = 0.64 \pm 0.05$.
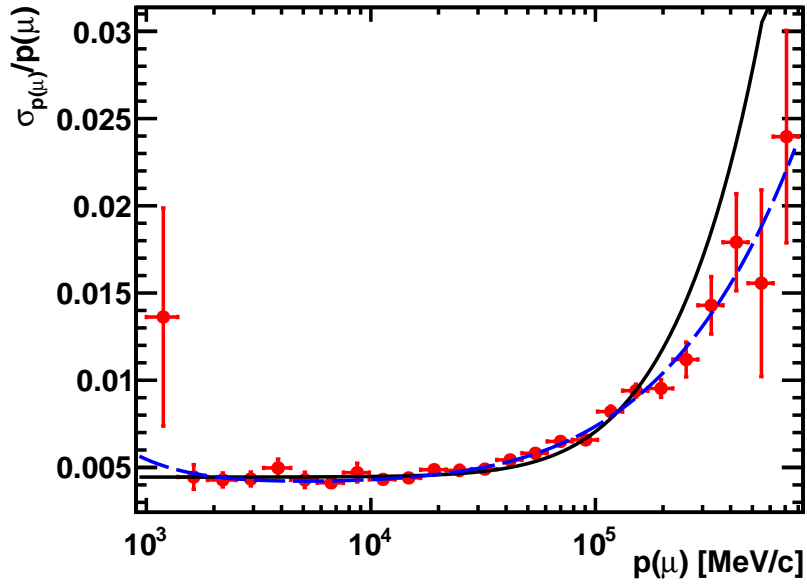


**Figure 5.2:** Relative momentum error of muons from Drell-Yan Monte Carlo as a function of their momentum. The black solid (–) line shows the fit with the standard Gluckstern formula (Eq. 5.1) while the blue dashed (- -) line shows the fit with the modified Gluckstern formula Eq. (5.2).

## 5.2 The Invariant Mass Resolution as a Function of the Invariant Dimuon Mass

### 5.2.1 Derivation from First Principles and the Gluckstern Formula

We use first principles of relativistic kinematics to estimate the shape of the invariant mass resolution. We start from the invariant dimuon mass $m_{\mu\mu}$:

$$
\begin{aligned}
m_{\mu\mu}^2 &= 2 \cdot p_{\mu^+}^\nu p_{\mu^-}^\rho g_{\nu\rho} + 2 \cdot m_\mu^2 \\
&= 2 \cdot \left( \sqrt{\vec{p_{\mu^+}}^2 + m_\mu^2} \cdot \sqrt{\vec{p_{\mu^-}}^2 + m_\mu^2} - \vec{p_{\mu^+}} \cdot \vec{p_{\mu^-}} \right) + 2 \cdot m_\mu^2
\end{aligned}
\tag{5.3}
$$

As $|\vec{p_\mu}| \gg m_\mu$ and $m_{\mu\mu} \gg m_\mu$ we can simplify (5.3) to

$$
m_{\mu\mu}^2 = 2 \cdot p_{\mu^+} \cdot p_{\mu^-} \cdot (1 - \cos\theta),
\tag{5.4}
$$

with $p_i = |\vec{p_i}|$ and $\theta$ as the angle between the two muons.

The error on the invariant mass will depend on the measurement errors of the two track momenta and the opening angle $\theta$. We can neglect in first approximation the error on $\theta$ as it propagates with $\sin\theta$ and as $\min(\cos\theta) \approx 0.83$ due to the acceptance of the detector and the large Lorentz boost. Therefore we obtain for the invariant mass resolution $\sigma_{m_{\mu\mu}}$ by error propagation

$$
\begin{aligned}
\sigma_{m_{\mu\mu}} &= \frac{1}{2} \cdot \frac{\sigma_{m_{\mu\mu}^2}}{m_{\mu\mu}} \\
&\approx \frac{m_{\mu\mu}}{2} \cdot \sqrt{\left( \frac{\sigma_{p_{\mu^+}}}{p_{\mu^+}} \right)^2 + \left( \frac{\sigma_{p_{\mu^-}}}{p_{\mu^-}} \right)^2}
\end{aligned}
\tag{5.5}
$$

If the magnitude of the two momenta is similar (i.e. $p_{\mu^+} \approx p_{\mu^+} \approx p_\mu$) we can state that $m_{\mu\mu} \propto p_\mu$. Inserting Eq. (5.2) and neglecting the constant term and the multiple scattering term – they are only relevant for low momenta – we obtain

$$
\sigma_{m_{\mu\mu}} = A' \cdot m_{\mu\mu}^{1+\gamma},
\tag{5.6}
$$

$$
\tag{5.7}
$$

with $\gamma = 1$ for the classical Gluckstern Formula and $\gamma = 0.64$ for the shape extracted in Sec. 5.1.

## 5.2.2 The Invariant Mass Resolution in Drell-Yan Monte Carlo

We check the validity of this derivation by looking again at a Drell-Yan Monte Carlo sample described in Sec. 5.1. Fig. 5.3 shows the invariant mass resolution as a function of the invariant mass. For each value of the invariant mass $\sigma_{m_{\mu\mu}}$ is extracted as the standard deviation of the distribution of differences between the reconstructed invariant mass and the true dimuon mass.
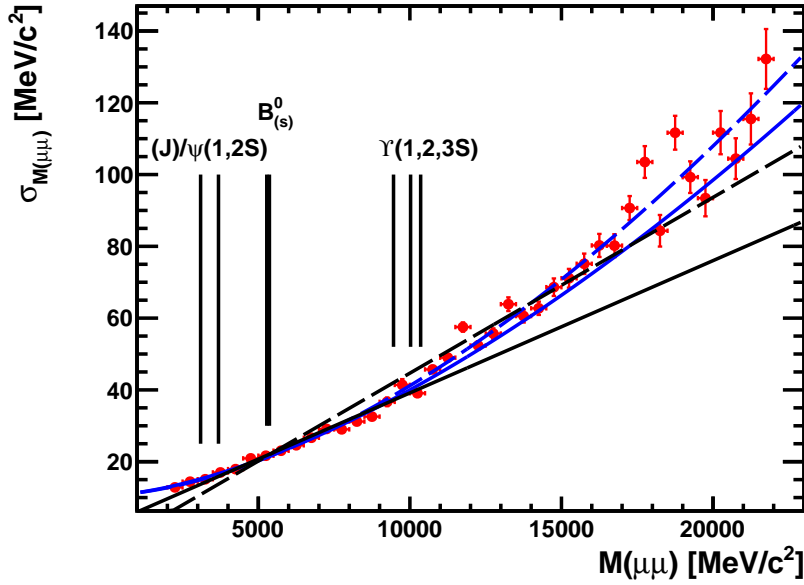


**Figure 5.3:** Invariant mass resolution from Drell-Yan Monte Carlo as a function of the invariant dimuon mass. The black lines show a linear fit to the full range (dashed, - -) and to the restricted range $m_{\mu\mu} \in [3,11]\,\text{GeV/c}^2$ of the charmonia and bottomia dimuon resonances (solid, –). The blue lines show a fit of a power law of the form (5.8) to the full range (dashed) and to the restricted range $m_{\mu\mu} \in [3,11]\,\text{GeV/c}^2$ (solid).

There is a strong correlation between the invariant mass of the muon pair and the momentum spectrum of the parent particle (i.e. the virtual photon in case of Drell-Yan production): A larger invariant mass shifts the spectrum to higher values. To remove this bias in the determination of $B^0_{(s)} \to \mu^+\mu^-$ invariant mass resolution, we split the considered $m_{\mu\mu} \in [2,22]\,\text{GeV/c}^2$ into bins of $0.5\,\text{GeV/c}^2$ and assign to every event within a given bin a weight such that the momentum spectra of parent particles in each bin correspond to the spectrum for $B^0_s \to \mu^+\mu^-$ extracted from Monte Carlo. To avoid a dominance of single events we introduce a maximal and minimal weighting of 10 and 1/10 respectively. Fig. 5.4 shows as an example the weighting process for the

bin $m_{\mu\mu} \in [6, 6.5]$ GeV/c$^2$. This weighting has been applied for the data shown in Fig. 5.3.
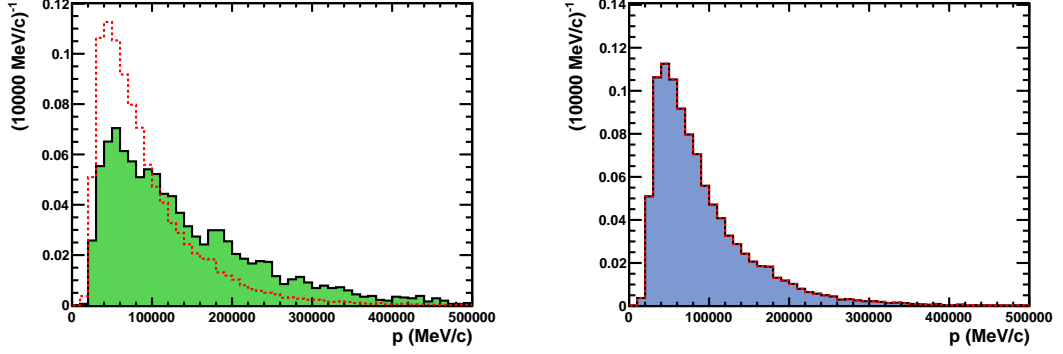


**Figure 5.4:** Scheme of the weighting procedure to match the momentum spectrum of the parent particle in Drell-Yan production to the one of $B_s^0 \to \mu^+\mu^-$ from Monte Carlo. Left: Unweighted spectrum of Drell-Yan production for $m_{\mu\mu} \in [7.0, 7.5]$ GeV/c$^2$, Right: Weighted spectrum of Drell-Yan production for $m_{\mu\mu} \in [7.0, 7.5]$ GeV/c$^2$. In both histograms, the red dashed line indicates the $B_s^0 \to \mu^+\mu^-$ Monte Carlo.

Fig. 5.3 shows that the invariant mass resolution is reasonably well approximated by linear function in the region of the Charmonium and Bottomium resonances (i.e. $m_{\mu\mu} \in [3, 11]$ GeV/c$^2$). On the other hand we see that the linear approximation does not hold anymore if a larger invariant mass range is considered. The shape of the curve is better described by a power law:

$$\sigma_{m_{\mu\mu}} = a_1 \cdot m_{\mu\mu}^{1+\gamma} + a_0, \tag{5.8}$$

For the range of $m_{\mu\mu} \in [3, 11]$ GeV/c$^2$, the linear fit gives $\chi^2/\text{ndf} = 22.24/14$ while the power law gives leads to $\chi^2/\text{ndf} = 13.03/13$. Over the full range the fit qualities are in case of the linear function $\chi^2/\text{ndf} = 243.11/38$ and in case of the power law gives $\chi^2/\text{ndf} = 66.35/37$.

The fit to the Drell-Yan Monte Carlo data in the range of $m_{\mu\mu} \in [2, 22]$ GeV/c$^2$ gives $\gamma = (0.67 \pm 0.04)$, in good agreement with the prediction of $\gamma = 0.64 \pm 0.05$ from the relative momentum error (obtained in Sec. 5.2.1).

We assign a systematic uncertainty on the estimated $B_{(s)}^0$ mass resolution due to the assumption of a linear invariant mass resolution by taking the difference of the predictions from a linear fit and from a power law fit over $m_{\mu\mu} \in [3, 11]$ GeV/c$^2$ to the Drell-Yan Monte Carlo data. These differences are $0.48$ MeV/c$^2$ at $m_{B_s^0}$ and $0.44$ MeV/c$^2$ at $m_{B^0}$.

## 5.2.3 The Invariant Mass Resolution in $J/\psi(1S)$, $\Upsilon(1S)$ and $Z^0$ Monte Carlo

We now use Monte Carlo $J/\psi(1S) \to \mu^+\mu^-$ and $\Upsilon(1S) \to \mu^+\mu^-$ samples to further study the interpolation method for the invariant mass resolution at $m_{B^0_{(s)}}$. We apply again the event weighting described in Sec. 5.2.2 on the two samples.

Fig. 5.5 and 5.6 show the invariant mass spectra of the two resonances after momentum weighting. They are fitted with a double Crystal Ball function (4.1). The invariant mass spectrum from Monte Carlo has already been shown in Fig. 4.2.

The parameters extracted from these fits are shown in Tab. 5.1 and 5.2.

**Table 5.1:** Parameters of the Crystal Ball fit to $J/\psi(1S) \to \mu^+\mu^-$ and $\Upsilon(1S) \to \mu^+\mu^-$ after momentum weighting. The values for $B^0_s \to \mu^+\mu^-$ from Monte Carlo are shown for comparison.

| Parameter | $J/\psi(1S)$ | $B^0_s$ | $\Upsilon(1S)$ |
|---|---|---|---|
| $\alpha_l$ | 1.25±0.03 | 1.56±0.04 | 1.31±0.04 |
| $\alpha_r$ | -1.61±0.03 | -1.40±0.07 | -1.49±0.04 |
| $n_l$ | 5.55±0.42 | 1.43±0.08 | 7.30±0.90 |
| $n_r$ | 4.69±0.31 | 9.80±2.00 | 5.60±0.50 |
| $\mu$ | 3097.62±0.06 MeV/c² | 5366.96±0.17 MeV/c² | 9461.98±0.17 MeV/c² |
| $\sigma$ | 12.08±0.05 MeV/c² | 18.75±0.15 MeV/c² | 30.41±0.15 MeV/c² |

**Table 5.2:** Parameters of the Crystal Ball fit to $J/\psi(1S) \to \mu^+\mu^-$ and $\Upsilon(1S) \to \mu^+\mu^-$ before momentum weighting. The values for $B^0_s \to \mu^+\mu^-$ from Monte Carlo are shown for comparison.

| Parameter | $J/\psi(1S)$ | $B^0_s$ | $\Upsilon(1S)$ |
|---|---|---|---|
| $\alpha_l$ | 1.93±0.03 | 1.56±0.04 | 1.21±0.04 |
| $\alpha_r$ | -1.64±0.04 | -1.40±0.07 | -1.37±0.03 |
| $n_l$ | 2.26±0.12 | 1.43±0.08 | 9.10±1.30 |
| $n_r$ | 3.98±0.29 | 9.80±2.00 | 7.11±0.07 |
| $\mu$ | 3097.34±0.06 MeV/c² | 5366.96±0.17 MeV/c² | 9462.27±0.18 MeV/c² |
| $\sigma$ | 11.79±0.05 MeV/c² | 18.75±0.15 MeV/c² | 32.68±0.17 MeV/c² |

The linear interpolation,

$$\sigma_{m_{\mu\mu}} = a_1 \cdot m_{\mu\mu} + a_0, \tag{5.9}$$

of the invariant mass resolution from $J/\psi(1S)$ and $\Upsilon(1S)$ is shown in Fig. 5.7. The parameters of the interpolation and the predicted invariant mass resolution for $B^0_s \to \mu^+\mu^-$ are displayed in Tab. 5.3.

We see that the estimated mass resolutions from the interpolation are in good agreement withthe one directly extracted from $B^0_s$ Monte Carlo ($\sigma_{m_{\mu\mu}} = 18.75 \pm 0.15$) when we
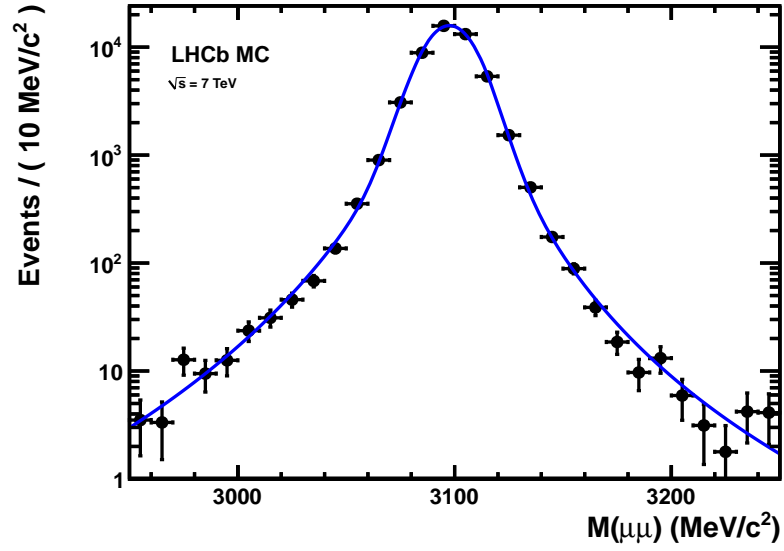
**Figure 5.5:** Invariant mass distribution for $J/\psi(1S) \to \mu^+\mu^-$ from Monte Carlo, after event weighting to match the $B_s^0$ momentum spectrum from $B_s^0 \to \mu^+\mu^-$. The used fit model is a double Crystal Ball function.
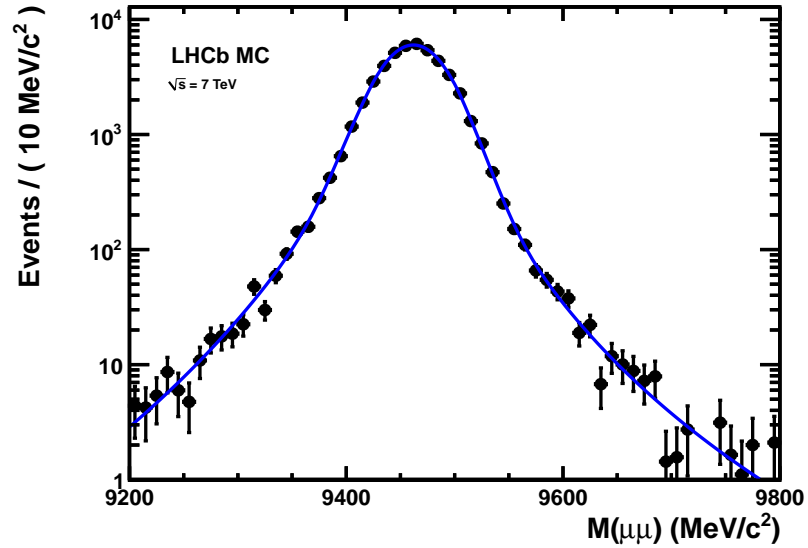


**Figure 5.6:** Invariant mass distribution for $\Upsilon(1S) \to \mu^+\mu^-$ from Monte Carlo, after weighting to match the $B_s^0$ momentum spectrum from $B_s^0 \to \mu^+\mu^-$. The used fit model is a double Crystal Ball function.
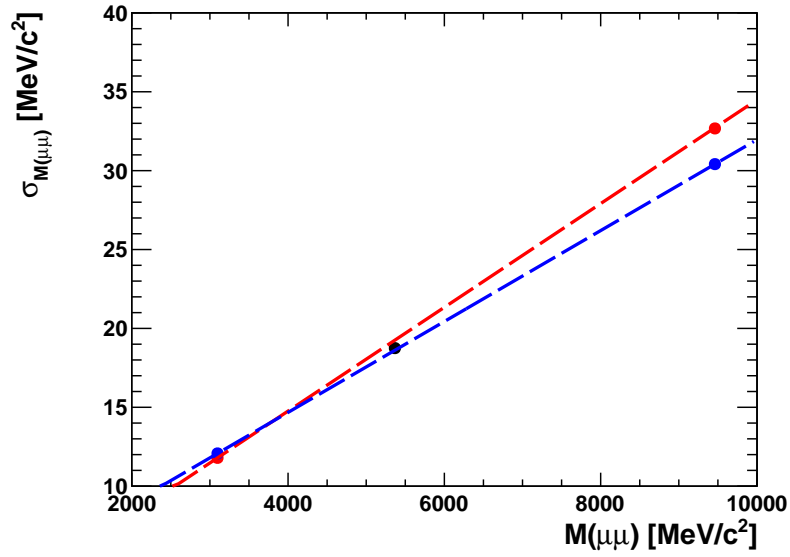
**Figure 5.7:** Linear interpolation of the invariant mass resolution from $J/\psi(1S)$ and $\Upsilon(1S)$ to $m_{B_s^0}$. The red dots and line show the invariant mass resolution determined without momentum weighting described in the text. The blue dots and line show invariant mass resolutions determined using momentum weighting. The black dot indicates the measured invariant mass resolution from $B_s^0 \to \mu^+\mu^-$ Monte Carlo.
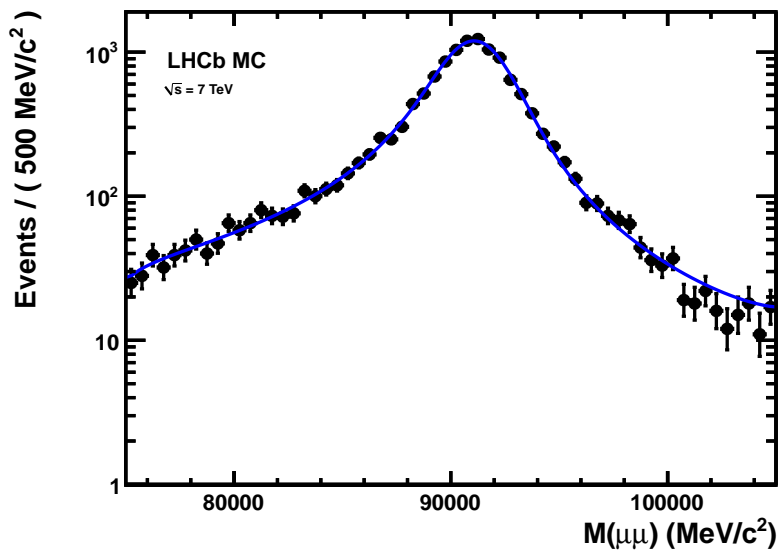


**Figure 5.8:** Invariant mass distribution for $Z^0 \to \mu^+\mu^-$ Monte Carlo. The fit model is a single Crystal Ball convolved with a Breit-Wigner function.

**Table 5.3:** Parameters of linear regression for the invariant mass resolution between $J/\psi(1S)$ and $\Upsilon(1S)$ and interpolated mass resolution for $B_s^0$

| Parameter | unweighted | weighted |
|---|---|---|
| $a_0$ | $1.61\pm 0.11\,\text{MeV}/\text{c}^2$ | $3.15\pm 0.11\,\text{MeV}/\text{c}^2$ |
| $a_1$ | $(3.29\pm0.03)\cdot10^{-3}$ | $(2.88\pm0.03)\cdot10^{-3}$ |
| correlation $\rho$ | -0.91 | -0.88 |
| $\sigma_{m_{\mu\mu},\text{pred.}}$ | $19.25\pm 0.07\,\text{MeV}/\text{c}^2$ | $18.61\pm 0.07\,\text{MeV}/\text{c}^2$ |

use the weighting method.

These result demonstrates that the interpolation method delivers a reliable prediction of the invariant mass resolution for $B_s^0 \rightarrow \mu^+\mu^-$. Furthermore, we see that the use of the weighting procedure gives a more precise result. It will therefore be used in the interpolation from data.

We look now at the $Z^0 \rightarrow \mu^+\mu^-$ Monte Carlo to check the interpolation over a wider invariant range. As the momentum spectrum of the $Z^0$ is completely different from the one of $B_s^0$, we can not apply the reweighting procedures. Therefore we look at the unweighted spectrum for all resonances.

The natural width of the $Z^0$ resonance is with $\Gamma_Z = 2.49\,\text{GeV}/\text{c}^2$ [25] of the same order of magnitude as the invariant mass resolution. Therefore we do not fit a simple Crystal Ball function, but a Crystal Ball function convolved with a Breit-Wigner function. The spectrum and fit are shown in Fig. 5.8 and the extracted parameters in Tab. 5.4.

**Table 5.4:** Fit parameters of $Z^0 \rightarrow \mu^+\mu^-$ from Monte Carlo

| Parameter | Value |
|---|---|
| $\alpha$ | $1.65\pm0.12$ |
| $n$ | $1.03\pm0.14$ |
| $\mu$ | $91.24\pm0.03\,\text{GeV}/\text{c}^2$ |
| $\sigma$ | $0.94\pm0.07\,\text{GeV}/\text{c}^2$ |
| $\Gamma$ | $2.49\pm0.09\,\text{GeV}/\text{c}^2$ |

Fig. 5.9 shows the invariant mass resolution from $J/\psi(1S)$, $\Upsilon(1S)$ and $Z^0$. We see that a linear extrapolation to the mass of $Z^0$ fails. The figure shows the power law fit to the unweighted Drell-Yan Monte Carlo (Eq. 5.8). This curve predicts the invariant mass resolution of $Z^0$ within its error.

## 5.2.4 Conclusion of Monte Carlo Studies

We conclude for these studies that the assumption of a linear dependence of the invariant mass resolution on the invariant mass is a valid approximation over the invariant
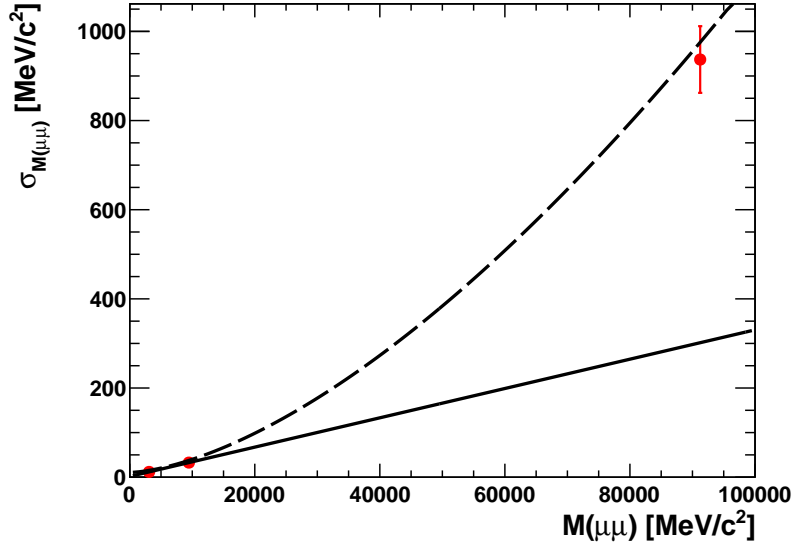
**Figure 5.9:** Invariant mass resolution of the $J/\psi(1S)$, $\Upsilon(1S)$ and $Z^0$ resonances. The black dashed (- -) line shows the power law fit from the Drell-Yan Monte Carlo without momentum weighting in the range $m_{\mu\mu} \in [3, 11]\,\text{GeV/c}^2$, the black solid (–) line the linear fit in the same range.

mass region from the Charmonium and Bottomium resonances. For the extraction of $\sigma_{m_{\mu\mu}}(m_{B_s^0})$ from data we will use a linear interpolation between the five considered resonances $J/\psi(1S)$ and $\psi(2S)$ as well as $\Upsilon(1S)$, $\Upsilon(2S)$ and $\Upsilon(3S)$. The limitation of five data points clustered in two groups discourages the use of a power law function.

## 5.3 The Invariant Mass Resolution from Data

After the Monte Carlo studies we are going to apply the interpolation method on data using the dimuon resonances $J/\psi(1S)$ and $\psi(2S)$ as well as $\Upsilon(1S)$, $\Upsilon(2S)$ and $\Upsilon(3S)$.

### 5.3.1 Data Samples and Selection

The data used in the following analysis is the whole 2010 data set. The dimuon candidates are built from two tracks meeting the requirement to be a muon[2]. In addition the

---

[2]A particle fulfills the so-called *IsMuon* requirement at LHC*b* if there is a certain number of muon station hits in a Field of Interest defined by the track extrapolation. The number of required hits is momentum dependent: $p \in [3, 6]\,\text{GeV/c}$: hits in M2 and M3, $p \in [6, 10]\,\text{GeV/c}$: hits in M2 and M3 as

tracks have to be of good fit quality ($\chi^2_{\text{track}}/\text{ndf} < 4$) and have a transverse momentum of the muon has to be larger than $p_T > 1000$ MeV/c. The fit quality requirement of the primary vertex fit has to have $\chi^2_{\text{PV}}/\text{ndf} < 10$.

We look at the charmonia ($J/\psi(1S)$ and $\psi(2S)$) and the bottomia ($\Upsilon(1S)$, $\Upsilon(2S)$ and $\Upsilon(3S)$) separately. The considered mass windows are $[2.9, 3.9]$ GeV/c$^2$ for charmonia and $[9, 11]$ GeV/c$^2$ for bottomia.

## 5.3.2 Dimuon Resonances and Interpolation

To each of the two data sets (charmonia and bottomia) we apply the momentum weighting procedure described in Sec. 5.2.2 to match the parent momentum spectra to the $B_s^0$ momentum spectrum in $B_s^0 \rightarrow \mu^+\mu^-$ Monte Carlo.

The invariant mass distribution for $J/\psi(1S)$ and $\psi(2S)$ is shown in Fig. 5.10, for $\Upsilon(1S)$, $\Upsilon(2S)$ and $\Upsilon(3S)$ in Fig. 5.11. The fit models for the resonances are double Crystal Ball functions having the transition points and exponents for both tails fixed to the values extracted from the Monte Carlo study (cf. Tab. 5.1, $J/\psi(1S)$ values for charmonia and $\Upsilon(1S)$ values for bottomia). Background is due to combinatorial background and Drell-Yan processes and is described by an exponential distribution.

The hit results for the mean $\mu$ and width $\sigma$ of the Crystal Ball functions as well as the relative signal yields $f_i$ of the resonances are shown in Tab. 5.5.

**Table 5.5:** Mean, width and relative yields of $J/\psi(1S)$ and $\psi(2S)$ as well as $\Upsilon(1S)$, $\Upsilon(2S)$ and $\Upsilon(3S)$ from data with momentum weighting of the dimuon system.

| Resonance | $\mu$ [MeV/c$^2$] | $\sigma$ [MeV/c$^2$] | $f_i$ |
|---|---|---|---|
| **Charmonia** | | | |
| $J/\psi(1S)$ | 3092.85±0.05 | 17.41±0.05 | 0.963±0.001 |
| $\psi(2S)$ | 3679.5 ±0.9 | 19.7± 0.5 | 0.037±0.001 |
| **Bottomia** | | | |
| $\Upsilon(1S)$ | 9451.7 ±0.4 | 46.3± 0.4 | 0.744±0.004 |
| $\Upsilon(2S)$ | 10013.2 ±1.0 | 48.9± 1.0 | 0.170±0.003 |
| $\Upsilon(3S)$ | 10341.8 ±1.9 | 56.2± 2.1 | 0.086±0.005 |

The linear interpolation between the extracted invariant mass resolutions is displayed in Fig. 5.12 where the solid horizontal black line shows the interpolated invariant mass resolution for $B_s^0$ and the horizontal dashed line shows the value for $B^0$. The values for the masses of the $B$ mesons are taken from the previous chapter (i.e. Eq. (4.6) and (4.7)). The red shaded band indicates the statistical error on the interpolated invariant mass resolution for $B_s^0$ and the grey shaded band shows the systematical error which is

---

well as in M4 or M5, $p > 10$ GeV/c: hits in M2, M3, M4 and M5 (cf. Ref. [17]).
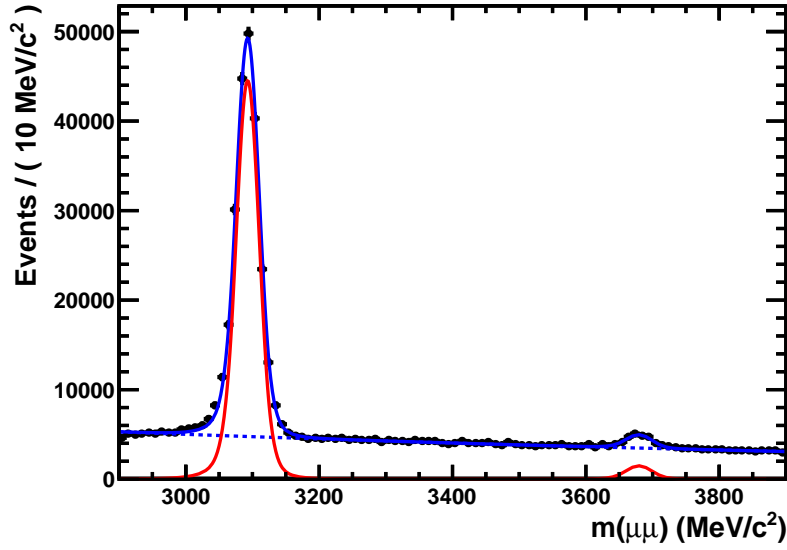
**Figure 5.10:** Dimuon invariant mass distribution showing $J/\psi(1S)$ and $\psi(2S)$ resonances. The distribution is described by two double Crystal Ball functions for the signal (red solid (–) line) and an exponential distribution for the combinatorial background (blue dashed (- -) line).
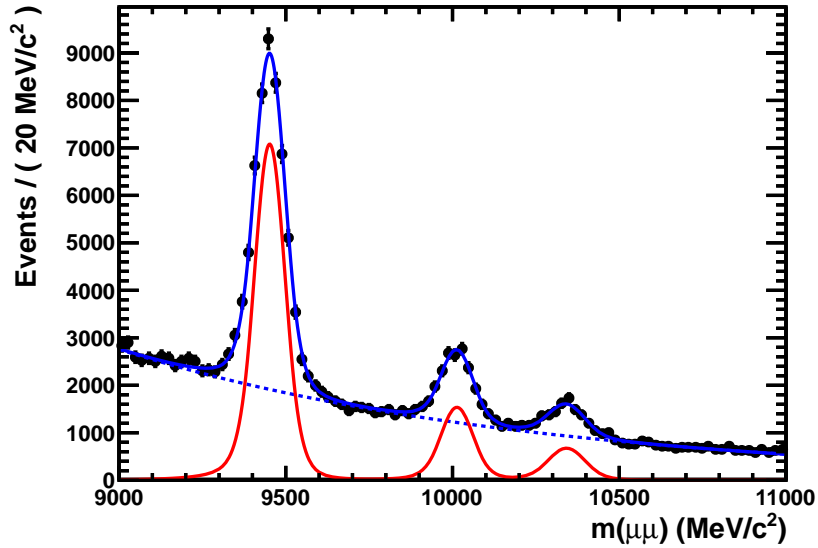


**Figure 5.11:** Dimuon invariant mass distribution showing $\Upsilon(1S)$, $\Upsilon(2S)$ and $\Upsilon(3S)$ resonances. The signal distribution is described by three double Crystal Ball functions for the signal (red solid (–) line) and an exponential distribution for the combinatorial background (blue dashed (- -) line).

discussed in detail below (Sec. 5.3.4).

The values for the interpolated invariant mass resolution and their statistical error are:

$$B^0 \to \mu^+\mu^- : \qquad \sigma = 27.4 \pm 0.3 \; \text{MeV/c}^2 \qquad\qquad (5.10)$$

$$B^0_s \to \mu^+\mu^- : \qquad \sigma = 27.8 \pm 0.3 \; \text{MeV/c}^2. \qquad\qquad (5.11)$$
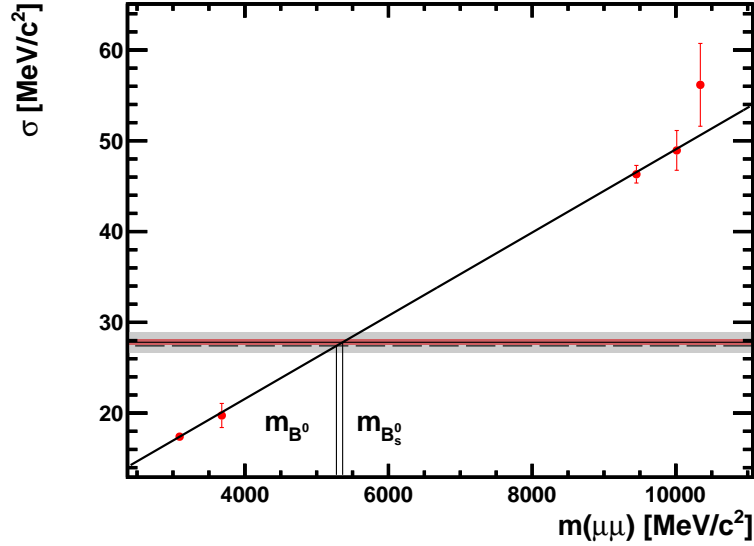


**Figure 5.12:** Interpolation of the Charmonia and Bottomia resonances from data (black thick solid line (–)). The thin black solid line shows the interpolated invariant mass resolution of 27.8 MeV/c$^2$ for $m_{B^0_s}$ together with the statistical error (red band) and the systematic error (grey band). The interpolated invariant mass resolution for $m_{B^0}$ (27.4 MeV/c$^2$) is indicated by the thin black long dashed (– –) line below the red band.

## 5.3.3 $Z^0$ **resonance**

As in the Monte Carlo section we study the shape of the invariant mass resolution derived from the inclusion of $Z^0 \to \mu^+\mu^-$. We have to use as already explained in the Monte Carlo section the non momentum-weighted data samples to get comparable results between the now in total six dimuon resonances.

For the $Z^0$ signal peak we use a single Crystal Ball function convolved with a Breit-Wigner distribution to describe the invariant mass distribution. The parameters of the radiative tail $\alpha$ and $n$ of the Crystal Ball are fixed to their values derived from Monte Carlo (cf. Tab. 5.4). Furthermore, we use an exponential function to describe the combinatorial background and the background from Drell-Yan processes.

Fig. 5.13 shows the measured invariant mass distribution and the maximum-likelihood fit while Tab. 5.6 lists the resulting fit parameters. The fit results in a value for $\Gamma$ which is in good agreement with the PDG value of 2.49 GeV/c$^2$ [25]. Tab. 5.7 lists the peak positions and the widths of all the six dimuon resonances.
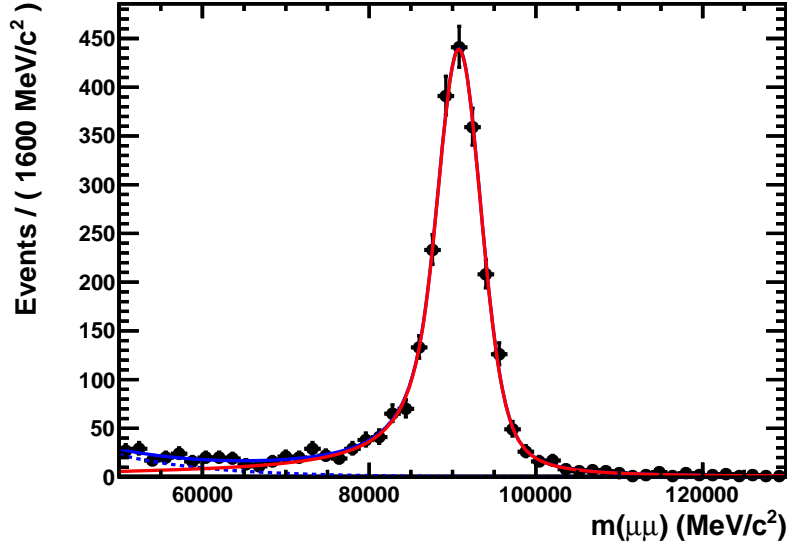


**Figure 5.13:** Invariant mass resolution for $Z^0 \to \mu^+\mu^-$ from data. The distribution is described by a convolution of a single Crystal Ball function and a Breit-Wigner function for the signal (red solid (–) line) and an exponential distribution for the combinatorial background (blue dashed (- -) line).

**Table 5.6:** Fit parameters of $Z^0 \to \mu^+\mu^-$ from data

| Parameter | Value |
|---|---|
| $\mu$ | $91.16 \pm 0.08$ GeV/c$^2$ |
| $\sigma$ | $2.19 \pm 0.15$ GeV/c$^2$ |
| $\Gamma$ | $2.36 \pm 0.25$ GeV/c$^2$ |

As already seen in the Monte Carlo study (cf. Sec. 5.2.3), the linear regression using the charmonia and bottomia resonances fails to predict the invariant mass resolution for $Z^0 \to \mu^+\mu^-$ (cf. Fig. 5.14). Like in Monte Carlo a better description is obtained by a power-law function.

The extracted exponent of the power law function $\beta = 1.62 \pm 0.32$ is in good agreement with the values derived in the Monte Carlo section from the Drell-Yan Monte Carlo (cf. Sec. 5.2) as well as the estimation from relative momentum errors (cf. Sec. 5.1).

It should be noted that we observe as in Chapter 4 for the $B^0_{(s)} \to h^+h^-$ a systematic shift in the measured peak positions of the dimuon resonances to lower values than the

**Table 5.7:** Mean, width and relative yields of the six considered dimuon resonances from fits to data without momentum weighting of the dimuon systems.

| Resonance | $\mu$ [MeV/c$^2$] | $\sigma$ [MeV/c$^2$] | $f_i$ |
|---|---|---|---|
| **Charmonia** | | | |
| $J/\psi(1S)$ | 3093.03$\pm$ 0.1 | 14.63$\pm$ 0.1 | 0.966$\pm$0.002 |
| $\psi(2S)$ | 3680.1 $\pm$ 1.0 | 17.2 $\pm$ 0.5 | 0.034$\pm$0.002 |
| **Bottomia** | | | |
| $\Upsilon(1S)$ | 9449.9 $\pm$ 0.4 | 50.6 $\pm$ 0.4 | 0.719$\pm$0.004 |
| $\Upsilon(2S)$ | 10013.0 $\pm$ 1.1 | 54.3 $\pm$ 1.1 | 0.184$\pm$0.003 |
| $\Upsilon(3S)$ | 10341.6 $\pm$ 2.0 | 60.4 $\pm$ 2.2 | 0.077$\pm$0.005 |
| $Z^0$ | 91160.0 $\pm$80.0 | 2190.0 $\pm$150.0 | 1.0 |
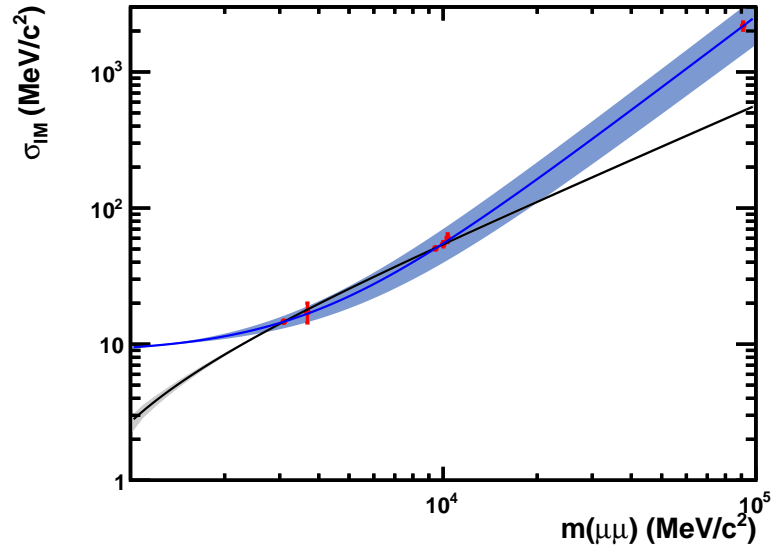


**Figure 5.14:** Invariant mass resolution of charmonia, bottomia and $Z^0$ resonances. The blue curve is the power law and the black one the linear function, both fitted to the charmonia and bottomia resonances. The bands indicate the error on the functions. At $m_{B^0_{(s)}}$ both functions agree within the errors. The power law extrapolates the invariant mass resolution of $Z^0$ within the error.

nominal masses [25]. Fig. 5.15 shows $\alpha = m_{\mathrm{meas}}/m_{\mathrm{PDG}}$ for all the fitted peak positions of the different particles. The values of obtained for the different resonances are in good agreement with each other. Their weighted average gives of $\alpha = 0.9989 \pm 0.0002$. This systematic shift is caused by scaling effects in the dipole magnet field and the alignment of the tracking system.
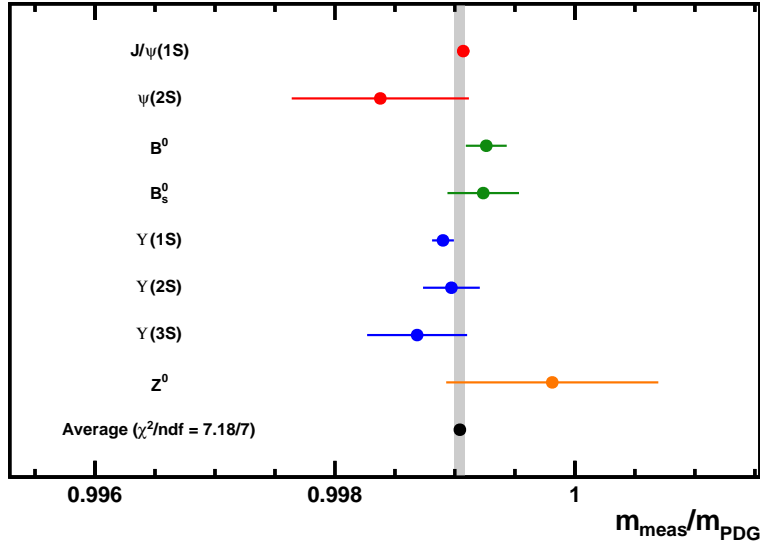


**Figure 5.15:** Ratio $\alpha$ of the measured to the nominal masses $m_{\mathrm{meas}}/m_{\mathrm{PDG}}$ for charmonia and bottomia dimuon resonances, $B^0 \rightarrow h^+ h^-$ and $B_s^0 \rightarrow h^+ h^-$ as well as $Z^0 \rightarrow \mu^+ \mu^-$.

## 5.3.4 Systematics

To estimate the systematics on the interpolated mass resolutions we check for the effects listed in the following. The assigned systematics are summarized in Tab. 5.8. The change in the interpolated mass resolutions are shown in the text.

1. **Selection cuts:** The systematics due to the selection cuts are studied by considering the resulting interpolation values if we change individually one of the three selection cuts on the transverse muon momentum, the track fit quality and the primary vertex fit quality. The cut on transverse momentum was changed to $p_T > 1200\,\mathrm{MeV/c}$ ($B_s^0 : \sigma = 27.59\,\mathrm{MeV/c^2}$, $B^0 : \sigma = 27.22\,\mathrm{MeV/c^2}$) and $p_T > 800\,\mathrm{MeV/c}$ ($B_s^0 : \sigma = 27.72\,\mathrm{MeV/c^2}$, $B^0 : \sigma = 27.41\,\mathrm{MeV/c^2}$), the track fit quality cut was altered to $\chi^2_{\mathrm{track}}/\mathrm{ndf} < 3$ ($B_s^0 : \sigma = 27.61\,\mathrm{MeV/c^2}$, $B^0 : \sigma = 27.25\,\mathrm{MeV/c^2}$) and $\chi^2_{\mathrm{track}}/\mathrm{ndf} < 5$ ($B_s^0 : \sigma = 27.46\,\mathrm{MeV/c^2}$, $B^0 : \sigma = 27.79\,\mathrm{MeV/c^2}$) and the cut on the primary vertex fit quality was changed to $\chi^2_{\mathrm{PV}}/\mathrm{ndf} < 8$ ($B_s^0 : \sigma =$

27.42 MeV/c$^2$, $B^0 : \sigma = 27.68$ MeV/c$^2$) and $\chi^2_{PV}$ / ndf < 12 ($B^0_s : \sigma = 27.39$ MeV/c$^2$, $B^0 : \sigma = 27.66$ MeV/c$^2$).

2. **Weighting procedure:** We estimate the systematics due to the weighting procedure by using on one hand an alternative method. This method removes or multiplies events such that it adapts the momentum spectrum of $B^0_s \rightarrow \mu^+\mu^-$ for the parent particle ($B^0_s : \sigma = 27.27$ MeV/c$^2$, $B^0 : \sigma = 26.73$ MeV/c$^2$). On the other hand the value for the maximal/minimal weighting was changed to (5,1/5) ($B^0_s : \sigma = 27.45$ MeV/c$^2$, $B^0 : \sigma = 27.02$ MeV/c$^2$) and (20,1/20) ($B^0_s : \sigma = 27.71$ MeV/c$^2$, $B^0 : \sigma = 27.32$ MeV/c$^2$) respectively. The deviations of the two checks were then quadratically added.

3. **Fit model:** Two tests are performed to estimate the systematics due to the fit model for the invariant mass distributions.
   In the first test, the peak distribution is described by a single Crystal Ball function with a left hand tail only and at the same time releasing the tail parameters from their values derived from Monte Carlo ($B^0_s : \sigma = 27.34$ MeV/c$^2$, $B^0 : \sigma = 27.82$ MeV/c$^2$).
   In the second test, the maximum-likelihood fit is split into two steps: In the first step, the background model (exponential distribution) is fitted from the sidebands of the invariant mass distributions, where we define the sidebands as the areas at least 80 MeV/c$^2$ (160 MeV/c$^2$) away from any of the charmonium (bottomium) resonances. The exponential parameter is fixed for the second step, in which we fit the resonances with a double Crystal Ball function where all parameters are free. In this way we avoid on the correlation between the exponential parameter of the background and the tail parameters of the Crystal Ball function ($B^0_s : \sigma = 26.92$ MeV/c$^2$, $B^0 : \sigma = 27.36$ MeV/c$^2$).
   The deviations of the derived invariant mass resolution for $B^0_{(s)}$ from these two checks are taken as systematic uncertainty by quadratically adding them.
   As a further check we fit – after extracting the background from the sidebands – the mass peaks with a gaussian but only using the data point above the transition points of the left-hand tail $\alpha_l$ extracted from Monte Carlo. This allows us to check the influence of a possible bias on the width of the gaussian arising from an imperfect description of the left-hand radiative tail by the Crystal Ball function. The influence of this modification on the width of the gaussian turns out to be small and is therefore neglected.

4. **Different statistical errors:** Due to the large differences in statistics among the resonances the interpolation is dominated by the $J/\psi(1S)$ and $\Upsilon(1S)$ resonances which have much smaller statistical errors on $\sigma$ than $\psi(2S)$, $\Upsilon(2S)$ and $\Upsilon(3S)$. The systematics of this dominance is estimated from the change in the interpolated invariant mass resolutions if the errors on the resolutions of the different

resonances are set to a common value (the magnitude of the error does not have an influence on a linear regression) and the error of the positions of the resonances along the invariant mass axis is set to zero ($B_s^0 : \sigma = 26.94\,\mathrm{MeV/c^2}$, $B^0 : \sigma = 27.32\,\mathrm{MeV/c^2}$).

5. **Mass window:** The value of the invariant mass resolution changes within the mass windows of $\pm 60\,\mathrm{MeV/c^2}$ around the $B_{(s)}^0$ masses, which are used for the $B_{(s)}^0 \to \mu^+\mu^-$ analysis. The change of the linear interpolated value over $60\,\mathrm{MeV/c^2}$ is included as a systematic uncertainty.

6. **Assumption of linear dependence of invariant mass resolution on the invariant mass:** The systematic uncertainty assigned due to this assumption is the one derived from the Drell-Yan Monte Carlo study described in Sec. 5.2.2.

**Table 5.8:** Systematic uncertainties on the interpolation method using dimuon resonances to estimate the invariant mass resolution at $m_{B^0}$ and $m_{B_s^0}$

| Systematic uncertainties | Value $B^0$ | Value $B_s^0$ |
|---|---|---|
| Selection cuts | $\pm 0.38$ MeV/c$^2$ | $\pm 0.21$ MeV/c$^2$ |
| Weighting procedure | $\pm 0.61$ MeV/c$^2$ | $\pm 0.53$ MeV/c$^2$ |
| Fit model | $\pm 0.50$ MeV/c$^2$ | $\pm 0.58$ MeV/c$^2$ |
| Asymmetric statistical errors | $\pm 0.23$ MeV/c$^2$ | $\pm 0.39$ MeV/c$^2$ |
| Mass window | $\pm 0.27$ MeV/c$^2$ | $\pm 0.27$ MeV/c$^2$ |
| Assumption of linear characteristic | $\pm 0.44$ MeV/c$^2$ | $\pm 0.48$ MeV/c$^2$ |
| Total systematic | $\pm 1.04$ MeV/c$^2$ | $\pm 1.06$ MeV/c$^2$ |

The systematic uncertainties are combined by summing them quadratically as there is no significant correlation among them. The total systematic uncertainty assigned to the interpolated invariant mass resolution for $B_s^0 \to \mu^+\mu^-$ ($B^0 \to \mu^+\mu^-$) is $1.1\,\mathrm{MeV/c^2}$ ($1.0\,\mathrm{MeV/c^2}$).

The final results of the interpolation method are therefore:

$$B^0 \to \mu^+\mu^- : \qquad \boxed{\sigma = 27.4 \pm 0.3 \text{ (stat.)} \pm 1.0 \text{ (syst.) MeV/c}^2} \qquad (5.12)$$

$$B_s^0 \to \mu^+\mu^- : \qquad \boxed{\sigma = 27.8 \pm 0.3 \text{ (stat.)} \pm 1.1 \text{ (syst.) MeV/c}^2} \qquad (5.13)$$

# 6 Invariant Mass Resolution from $B^0_{(s)} \to h^+ h^-$

In this chapter we extract the expected $B^0_{(s)} \to \mu^+ \mu^-$ invariant mass resolution from decays of $B^0$ and $B^0_s$ into two charged kaons or pions. These decays are similar in topology and kinematics to the $B^0_{(s)} \to \mu^+ \mu^-$ decays.

## 6.1 Separation of Different Decay Modes using RICH Information

There are – as already shown in Chapter 4 – in total four different decay modes of $B^0_{(s)}$ decaying into two kaons or pions [25]:

$$
\begin{aligned}
B^0 &\to \pi^+ \pi^- & \mathcal{B} &= (5.13 \pm 0.24) \cdot 10^{-6} \\
B^0_{(s)} &\to \pi^+ K^- & \mathcal{B} &= (1.94 \pm 0.06) \cdot 10^{-5} \, (B^0), = (4.9 \pm 1.0) \cdot 10^{-6} \, (B^0_s) \\
B^0_{(s)} &\to K^+ \pi^- & \mathcal{B} &= (1.94 \pm 0.06) \cdot 10^{-5} \, (B^0), = (4.9 \pm 1.0) \cdot 10^{-6} \, (B^0_s) \\
B^0_s &\to K^+ K^- & \mathcal{B} &= (3.3 \pm 0.9) \cdot 10^{-5}
\end{aligned}
$$

$$(6.1)$$

To assign the correct mass hypothesis for the final state particles in the reconstruction of the $B$ meson, we have to identify the kaons and pions by using the information from the two RICH detectors.

As explained in Chapter 4, the significance of a certain particle hypothesis $i$ against another hypothesis $j$ is represented by the Delta log-likelihood variable $\mathrm{DLL}_{i-j}$. The ratio between the probability that the particle $h$ is of type $i$ to the probability that the particle is of type $j$, is given by:

$$
\frac{p_i(h)}{p_j(h)} = \exp(\mathrm{DLL}_{i-j}). \tag{6.2}
$$

The $DLL_{K-\pi}$ variable is mainly based on information from the RICH detectors, i.e. the comparison of the detected Cherenkov ring to the expected for a kaon or a pion with momentum $p$ measured by the tracking system. As shown in Fig. 6.1 and 6.2, the separation power is strongly dependent on $p$. Therefore applying cuts on the $DLL_{K-\pi}$ variable leads to implicit cuts on the track momentum: Particles with very high momentum are more likely to be cut away than particles with lower momentum. This biases the observed invariant mass resolution.
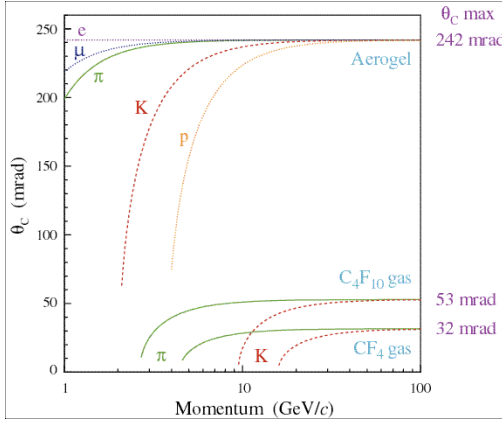


**Figure 6.1:** The Cherenkov angle of the three radiators used in LHC*b* (RICH1: Aerogel and $C_4F_{10}$; RICH2: $CF_4$) as a function of the track momentum and the particle hypotheses. The separation of the different hypotheses is decreasing with increasing momentum [23].
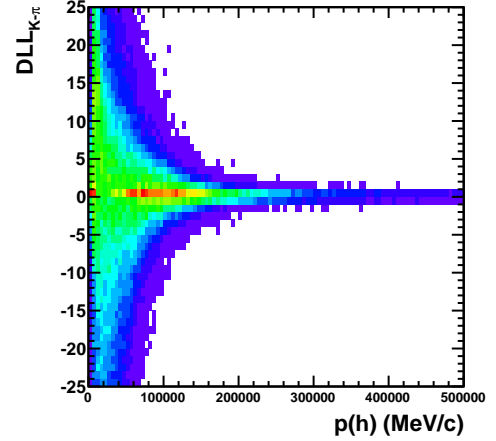
**Figure 6.2:** The track momentum $p$ versus the $DLL_{K-\pi}$ of the charged particles in two hadronic body decays. A cut of $|DLL_{K-\pi}| > 6$ corresponds defacto to a cut of about $p < 150$ GeV/c.

Other distributions that can be biased by a cut on the $DLL_{K-\pi}$ variable are the transverse momentum $p_T$ and the pseudorapidity $\eta$ of the particle[1] as well as the number of charged tracks and the number of primary vertices in the event. These dependencies are shown in Fig. 6.3.

Therefore applying cuts on the $DLL_{K-\pi}$ variable we have to correct for the efficiency of this cut in bins of these affected variables in order to remove the bias on the invariant mass distribution, especially on the invariant mass resolution.

---

[1]Note that $p$, $p_T$ and $\eta$ are linked by $\eta = \frac{1}{2} \log \left( \frac{p + \sqrt{p^2 - p_T^2}}{p - \sqrt{p^2 - p_T^2}} \right)$
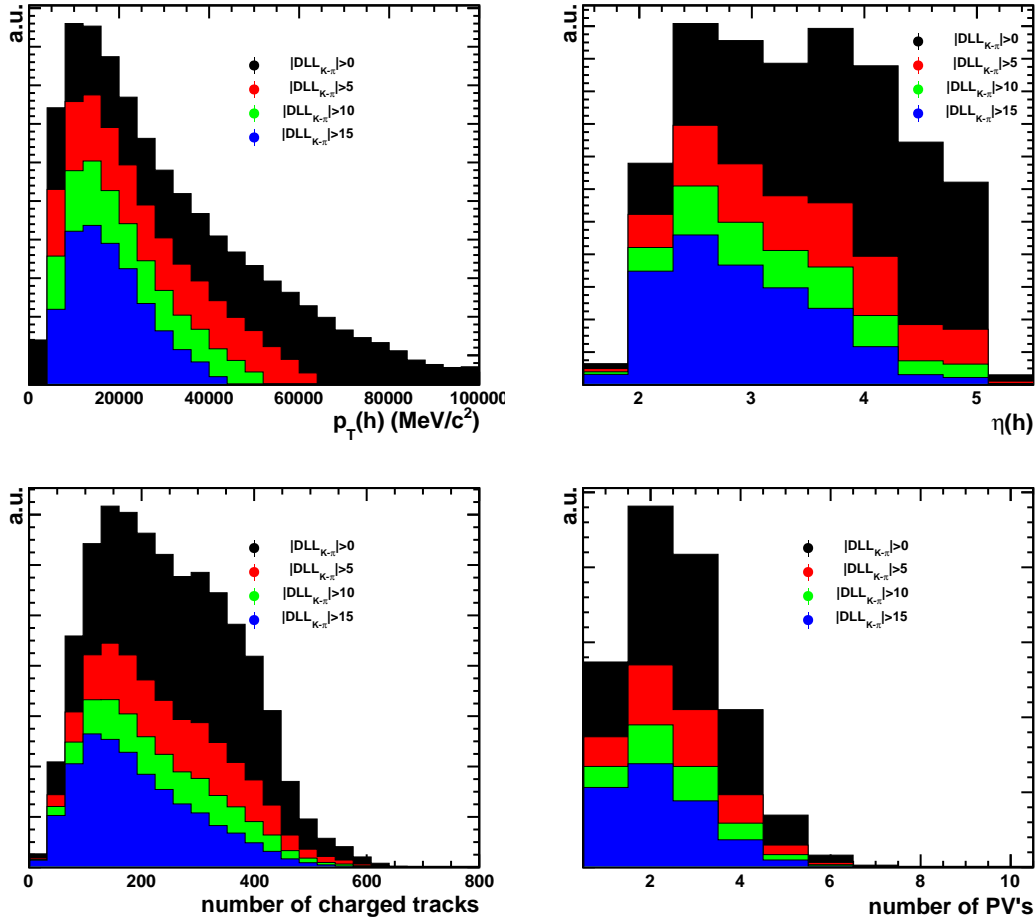
**Figure 6.3:** Distributions of track transverse momentum $p_T$ (top left), track pseudorapidity $\eta$ (top right), number of charged tracks in the event (bottom left) and number of primary vertices (bottom right) distributions for different cuts on $|\mathrm{DLL}_{K-\pi}|$

# 6.2 Determination of the RICH Efficiency

## 6.2.1 Variable Binning

The determination of the RICH efficiency should ideally be done in bins for all the variables listed above. Due to the limited statistics in the 2010 data set which is used in this analysis we restrict ourselves to those variables having the largest impact on the invariant mass resolution. These are the track momentum and the track transverse momentum.

Following bins in $p$ and $p_T$ were chosen:

$p$ binning: $\quad [2, 5, 10^a, 16^b, 20, 23, 26, 30, 60^c, 105, 150]$ GeV/c

$p_T$ binning: $\quad [0.5, 5, 50]$ GeV/c $\hspace{4cm}$ (6.3)

$\qquad\qquad$ The marked bins correspond to the boundaries of the different radiators:

$\quad^a\quad$ Upper threshold of the Aerogel radiator

$\quad^b\quad$ Lower threshold of the CF$_4$ radiator

$\quad^c\quad$ Upper threshold of the C$_4$F$_{10}$ radiator [23]

## 6.2.2 Extraction of the RICH Efficiency

The chosen binning scheme gives 20 ($= 2 \times 10$) two-dimensional bins in which we determine the RICH efficiency and its error for different cuts on DLL$_{K-\pi}$. As an example, Fig. 6.4 shows the kaon and pion identification efficiencies in bins of $p$ and $p_T$ for different cuts on DLL$_{K-\pi}$. The used calibration data comes from the decay modes $D^{*+} \rightarrow D^0(K^-\pi^+)\pi^+$ and $D^{*-} \rightarrow \overline{D}^0(K^+\pi^-)\pi^-$ where the soft pion is assumed to come from the decay of the $D^*$ meson for tagging. Kaons and pions can be identified in these decay modes by charge. Further the modes have the advantage of a large statistic and of having very low background. Therefore the efficiency determination can base on a counting method: The efficiency is the ratio of the number of events passing the DLL$_{K-\pi}$ cut to the number of total events in the considered $(p, p_T)$-bin. The error on the efficiency is based on the statistical error, but takes into account possible contamination from background.
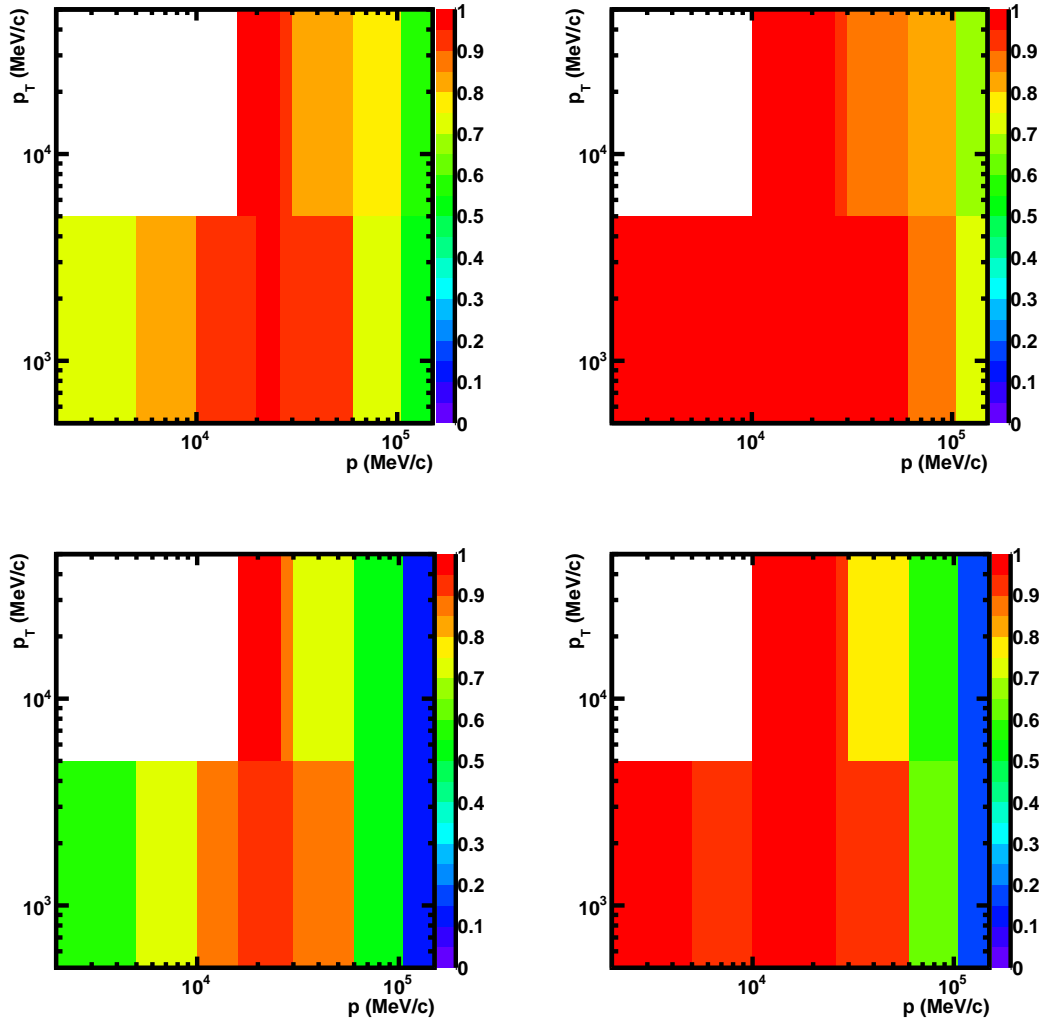
**Figure 6.4:** Reconstructed RICH efficiencies for pions (left) and kaons (right) in bins of $p$ and $p_T$, for a cut of $\text{DLL}_{K-\pi} < 0$ (pions) and $\text{DLL}_{K-\pi} > 0$ (kaons) in the top row and for a cut of $\text{DLL}_{K-\pi} < -3$ (pions) and $\text{DLL}_{K-\pi} > 3$ (kaons) in the bottom row. The efficiency scale is linear from 0.0 (violet) to 1.0 (red). The white area represents the kinematically not allowed region $p < p_T$.

# 6.3 Invariant Mass Distribution with Efficiency Corrected

To estimate the unbiased invariant mass resolution for $B^0_{(s)} \to h^+ h^-$ we look at the invariant mass distribution for different cuts $\kappa$ on $\mathrm{DLL}_{K-\pi}$. For a given value $\kappa$ we identify a particle $h$ as a kaon if $\mathrm{DLL}_{K-\pi}(h) > \kappa$ and as a pion if $-\mathrm{DLL}_{K-\pi} > \kappa$. We do this for both final state particles in the decay and assign each event to one of the four decay modes and to the corresponding mass hypothesis according to (6.4).

$$
\begin{aligned}
B^0 \to \pi^+ \pi^- &\quad \text{if} \quad -\mathrm{DLL}_{K-\pi}(h^+) > \kappa &\&&\quad -\mathrm{DLL}_{K-\pi}(h^+) > \kappa \\
B^0_{(s)} \to \pi^+ K^- &\quad \text{if} \quad -\mathrm{DLL}_{K-\pi}(h^+) > \kappa &\&&\quad \mathrm{DLL}_{K-\pi}(h^-) > \kappa \\
B^0_{(s)} \to K^+ \pi^- &\quad \text{if} \quad \mathrm{DLL}_{K-\pi}(h^+) > \kappa &\&&\quad -\mathrm{DLL}_{K-\pi}(h^-) > \kappa \\
B^0_s \to K^+ K^- &\quad \text{if} \quad \mathrm{DLL}_{K-\pi}(h^+) > \kappa &\&&\quad \mathrm{DLL}_{K-\pi}(h^-) > \kappa
\end{aligned}
$$

$$(6.4)$$

For $\kappa > 0$ we obtain for every accepted event a well-defined mass hypothesis.

Due to the relatively small size of the data sample we will not look at the different decay modes individually, but at an inclusive invariant mass distribution of $B^0_{(s)} \to h^+ h^-$. The used data sample is the same as described in Sec. 4.1.1. In addition we apply a cut on the Geometrical Likelihood of $GL > 0.2$ to reduce the background.

We only consider events where both particles fulfill $p \in [2, 150]$ GeV/c and $p_T \in [0.5, 50]$ GeV/c. This restriction implies a bias on the invariant mass resolution which we correct for by introducing a correction factor $\gamma$. We use two different data samples to check this correction factor: We determine $\gamma$ as the ratio between the invariant mass resolutions with and without these cuts on $p$ and $p_T$. $\gamma$ is extracted on one hand from a $B^0_s \to \mu^+ \mu^-$ Monte Carlo sample as the ratio between the widths of the double Crystal Ball functions fitted to the invariant mass distributions ($\gamma = 1.027 \pm 0.013$). On the other hand we determine $\gamma$ from the invariant mass resolution using the interpolation method applied on data described in Chapter 5 ($\gamma = 1.043 \pm 0.015$), where we apply the cuts on $p$ and $p_T$ on the dimuon resonances. The results from both methods are in good agreement and we take the weighted average of

$$\gamma = 1.034 \pm 0.009. \tag{6.5}$$

When creating the $B^0_{(s)} \to h^+ h^-$ invariant mass distribution, a weight $w$ depending on the estimated particle identification efficiency as a function of $p$ and $p_T$ of the two

involved final states particle defined by (6.6) is assigned to every event.

$$
w = \begin{cases}
\dfrac{1}{\varepsilon_\pi(p(h^+),p_T(h^+),\kappa)\cdot\varepsilon_\pi(p(h^-),p_T(h^-),\kappa)} & \text{if} - \text{DLL}_{K-\pi}(h^+) > \kappa \,\&\, -\text{DLL}_{K-\pi}(h^-) > \kappa, \\[2ex]
\dfrac{1}{\varepsilon_\pi(p(h^+),p_T(h^+),\kappa)\cdot\varepsilon_K(p(h^-),p_T(h^-),\kappa)} & \text{if} - \text{DLL}_{K-\pi}(h^+) > \kappa \,\&\, \text{DLL}_{K-\pi}(h^-) > \kappa, \\[2ex]
\dfrac{1}{\varepsilon_K(p(h^+),p_T(h^+),\kappa)\cdot\varepsilon_\pi(p(h^-),p_T(h^-),\kappa)} & \text{if}\, \text{DLL}_{K-\pi}(h^+) > \kappa \,\&\, -\text{DLL}_{K-\pi}(h^-) > \kappa, \\[2ex]
\dfrac{1}{\varepsilon_K(p(h^+),p_T(h^+),\kappa)\cdot\varepsilon_K(p(h^-),p_T(h^-),\kappa)} & \text{if}\, \text{DLL}_{K-\pi}(h^+) > \kappa \,\&\, \text{DLL}_{K-\pi}(h^-) > \kappa,
\end{cases}
\tag{6.6}
$$

where $\varepsilon_\pi$ is the efficiency for pions and $\varepsilon_K$ is the efficiency for kaons.

Events, where one of the two particles falls into a $(p, p_T)$-bin for which the efficiency is $\varepsilon < 0.005$, are skipped to avoid dominance by single events. As shown later, this procedure leads to a bias on the estimated invariant mass resolution if strong cuts on the DLL variable are applied. Therefore results obtained for strong cuts on the DLL value are not taken into account for the extraction of the invariant mass resolution.

The invariant mass distribution is shown in Fig. 6.5 for $\kappa = 0$ and in Fig. 6.6 for $\kappa = 3$. To extract the invariant mass resolution from the invariant mass distributions we perform a maximum likelihood fit assuming the following model:

- **Signal:** Two double Crystal Ball functions ($B^0$ and $B_s^0$) with the parameters $\alpha_{l,r}$ and $n_{l,r}$ fixed to the values obtained from a fit to a large $B^0_{(s)} \to K^\pm \pi^\mp$ Monte Carlo sample and a common width $\sigma_{IM}$ of the gaussian being taken as the invariant mass resolution.

- **Physical background:** Contributions from the decay modes $\Lambda_b^0 \to p^\pm K^\mp / \pi^\mp$ where the (anti-)proton is misidentified as a kaon (or a pion) are described by a gaussian with a variable mean and a width that is constrained to be larger than 30 MeV/c$^2$.
  Contributions from the decay modes $B \to hhh$ where one track is missed are also described by a gaussian with a variable mean and a width that is constrained to be larger than 50 MeV/c$^2$[2].

- **Combinatorial background:** The combinatorial background is described by an exponential distribution.

---

[2]We use a different description for this contribution here than in Sec. 4.2 (cf. [15]) because the efficiency correction changes the shape of the physical background from $B \to hhh$ contribution. This is because the involved final state particles tend to have lower momenta than the particles in $B^0_{(s)} \to h^+ h^-$ .

**Figure 6.5:** Invariant $h^+ h^-$ mass distribution for $|\mathrm{DLL}_{K-\pi}| > 0$ and the corresponding maximum likelihood fit. The signal peaks are displayed by the red solid (–) line, the physical background as black dashed (- -) line and the combinatorial background as blue dashed line. The contribution from the decay $\Lambda^0_b \to p^\pm K^\mp / \pi^\mp$ is not visible.
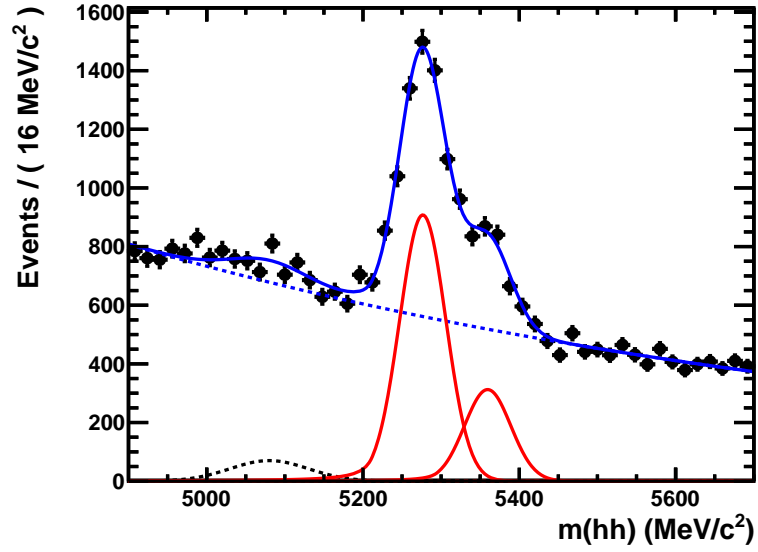


**Figure 6.6:** Invariant $h^+ h^-$ mass distribution for $|\mathrm{DLL}_{K-\pi}| > 3$ and the corresponding maximum likelihood fit. The signal peaks are displayed by the red solid (–) line, the physical background as black dashed (- -) line and the combinatorial background as blue dashed line. The contribution from the decay $\Lambda^0_b \to p^\pm K^\mp / \pi^\mp$ is not visible.
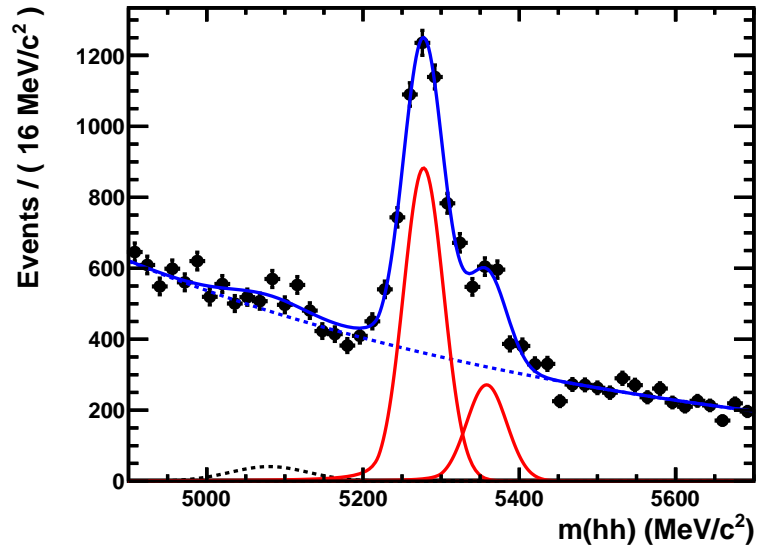
# 6.4 Invariant Mass Resolution as a Function of the $DLL_{K-\pi}$ Cut

We determine the invariant mass resolution $\sigma_{IM}$ as a function of the DLL cut $\kappa$ in a range of $\kappa \in [0, 10]$ in steps of 0.5. The result is displayed in Fig. 6.7.

As expected, the invariant mass resolution decreases with increasing $\kappa$ and seems to converge toward a value $\sigma_{unbias}$. We define this value as the unbiased invariant mass resolution. This decrease in $\sigma_{IM}$ is caused as with increasing $\kappa$ the fraction of events where one or even both particles are misidentified is decreasing. In principle, a contribution of events with wrong mass hypothesis leads to a too large width of the signal peaks.
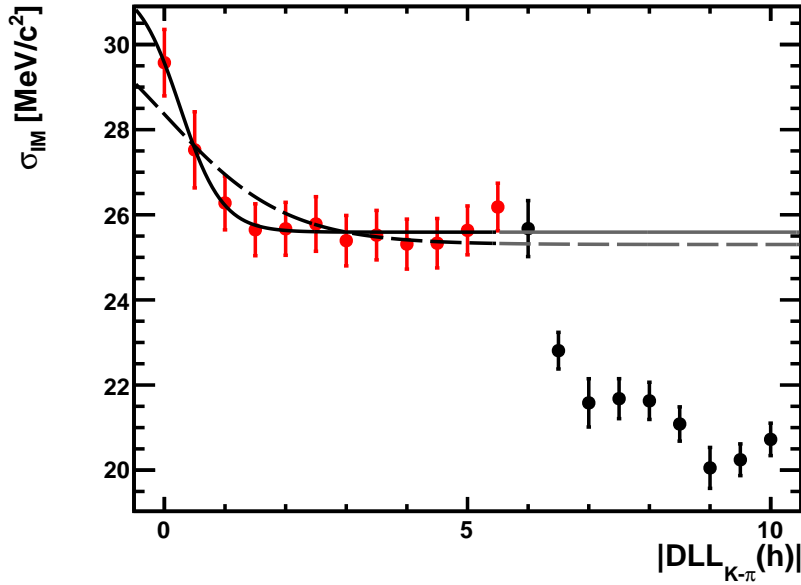


**Figure 6.7:** Invariant mass resolution as a function of the $DLL_{K-\pi}$ cut. The solid (–) line shows the fit model described in (6.7) while the dashed (- -) displays the same function with $\kappa_0 = r = 1$ (i.e. assuming the $DLL_{K-\pi}$ variable to be a perfect log-likelihood). The black data points indicate the range of the $DLL_{K-\pi}$ values not used for the fit.

At a value of $\kappa \approx 6$, $\sigma_{IM}$ drops abruptly. The reason is that all the particles in the highest part of the considered momentum spectrum ($[2, 150]$ GeV/c) do not pass such strong DLL cuts (cf. Fig. 6.2). This effect can not be corrected by the weighting procedure and leaves an unavoidable bias on the invariant mass resolution as events with lower momentum particles tend to have a smaller invariant mass resolution.
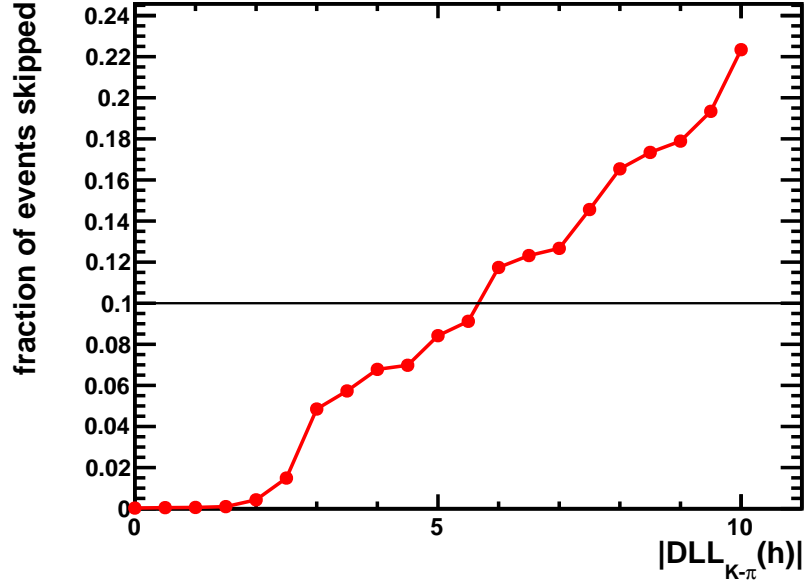
**Figure 6.8:** Fraction of skipped events with one of the particles in a $(p, p_T)$ bin with efficiency $\varepsilon < 0.005$ as a function of $\kappa$. The black line shows the defined threshold of 0.1. Only values for $\kappa \leq 5.5$ are included in the extraction of the unbiased invariant mass resolution.

The fraction of events which are skipped as they contain a particle falling into a $(p, p_T)$ bin, where the efficiency is $\varepsilon < 0.005$, is larger than 10% for $\kappa \geq 6$ (cf. Fig. 6.8). Therefore to extract $\sigma_{\text{unbias}}$ we take into account only the range of $\kappa \in [0, 5.5]$. We extract $\sigma_{\text{unbias}}$ by fitting the function

$$\sigma_{IM}(\kappa) = \sigma_{\text{unbias}} + \frac{\sigma_{\text{mis-ID}}}{1 + r \cdot \exp\left(\kappa / \kappa_0\right)}. \tag{6.7}$$

This function represents the two contributions to $\sigma_{IM}$: The actually unbiased invariant mass resolution and the contribution from misidentified final state particles. For the second contribution we take into account that the probability to misidentify a kaon as a pion is $p_{\text{mis-ID}} = 1 / (1 + \exp(\text{DLL}_{K-\pi}))$ and $p_{\text{mis-ID}} = 1 / (1 + \exp(-\text{DLL}_{K-\pi}))$ vice versa based on the definition of the delta log-likelihood (cf. (6.2)). The parameters $r$ and $\kappa_0$ represent the fact that the $\text{DLL}_{K-\pi}$ value is not a perfect log-likelihood. The fitted function is shown in Fig. 6.7, the fitted parameters are listed in Tab. 6.1.

In a last step we correct the extracted unbiased invariant mass resolution for the cuts on $p$ and $p_T$ by the correction factor $\gamma$

$$\sigma_{\text{unbias,corr}} = \sigma_{\text{unbias}} \cdot \gamma \tag{6.8}$$

**Table 6.1:** Fit parameters of $\sigma_{IM}(\kappa)$

| Parameter | Value |
|---|---|
| $\sigma_{\text{unbias}}$ | $25.59 \pm 0.21$ MeV/c$^2$ |
| $\sigma_{\text{mis-ID}}$ | $5.8 \pm 1.3$ MeV/c$^2$ |
| $\kappa_0$ | $0.35 \pm 0.38$ |
| $r$ | $0.53 \pm 0.75$ |

and obtain the final result of

$$\sigma_{\text{unbias,corr}} = (26.46 \pm 0.58) \text{ MeV/c}^2, \tag{6.9}$$

where the quoted error is the mean of the errors on $\sigma_{IM}$ for $\kappa \in [0, 5.5]$. We take this value rather than the error returned by the fit as the errors on $\sigma_{IM}$ for different values of $\kappa$ are strongly correlated.

## 6.5 Systematics and Final Result

Different potential sources for systematics have been studied. In the following we briefly describe these sources and how we estimate the corresponding uncertainties. The values for the systematic uncertainties are summarized in Tab. 6.2.

1. **GL cut:** The systematic error due to the cut on the Geometrical Likelihood is defined as the maximal deviation on $\sigma_{\text{unbias,corr}}$ if we choose a GL cut of 0.25 ($\sigma_{\text{unbias,corr}} = 25.83$ MeV/c$^2$) and of 0.15 ($\sigma_{\text{unbias,corr}} = 26.32$ MeV/c$^2$) instead of 0.20.

2. **Considered range of $\kappa$:** Systematic effects coming from the restriction to $\kappa \in [0, 5.5]$ are estimated by fitting the function (6.7) to the range $\kappa \in [0, 5]$ ($\sigma_{\text{unbias,corr}} = 26.68$ MeV/c$^2$) as well as $\kappa \in [0, 6]$ ($\sigma_{\text{unbias,corr}} = 26.37$ MeV/c$^2$). We take the maximal deviation to our result as systematic uncertainty.

3. **Steps in $\kappa$:** A systematic effect due to by the step size in $\kappa$ is determined by looking at the fit result of $\sigma_{IM}$ if we use a step sizes of 0.4 ($\sigma_{\text{unbias,corr}} = 26.20$ MeV/c$^2$), 0.6 ($\sigma_{\text{unbias,corr}} = 26.32$ MeV/c$^2$) and 1.0 ($\sigma_{\text{unbias,corr}} = 26.39$ MeV/c$^2$). We take the maximal deviation from $\sigma_{\text{unbias,corr}}$ with these three choices as systematic uncertainty. The range of $\kappa$ is left unchanged.

4. **Correction factor $\gamma$:** The error on $\gamma$ is taken by simple error propagation of (6.8) as systematic effect for this correction.

5. **Binning scheme of the efficiency determination:** The systematic uncertainty

due to the binning scheme of $p$ and $p_T$ is estimated by calculating $\sigma_{\text{unbias,corr}}$ in the three different binning schemes: One with only one bin in $p_T$ ($\sigma_{\text{unbias,corr}} = 25.83\,\text{MeV/c}^2$), one with the ten bins in $p$ uniformly distributed ($\sigma_{\text{unbias,corr}} = 25.37\,\text{MeV/c}^2$) and one with one bin in $p_T$ but as compensation two bins in $\eta$ ($\eta < 3.5$ and $\eta > 3.5$) bin ($\sigma_{\text{unbias,corr}} = 25.59\,\text{MeV/c}^2$). The maximal deviation in any of these three scenarios from the actual result is taken as the systematic effect on the invariant mass resolution.

6. **Fit function for the invariant mass distribution:** To check systematic effects due to the chosen fit function for the invariant mass distribution we use a simplified model where we do not include any physical background and use as signal distribution two left-handed Crystal Ball functions. This fit yields $\sigma_{\text{unbias,corr}} = 26.89\,\text{MeV/c}^2$ and the difference to the standard result (6.9) is used as the corresponding systematic uncertainty.

7. **Fit function for $\sigma_{IM}(\kappa)$:** The systematic due to the fit function $\sigma_{IM}(\kappa)$ is evaluated by using similar functions and taking the maximal deviation from the standard result (6.9). These functions are:

   - The function described in (6.7), but with $r = \kappa_0 = 1$, i.e. assuming $\text{DLL}_{K-\pi}$ is indeed a log-likelihood (cf. Fig. 6.7) ($\sigma_{\text{unbias,corr}} = 26.16\,\text{MeV/c}^2$).

   - The function described in (6.7) where the square root of the quadratical sum of the mis-ID part and the unbiased part is taken. This meets a convolution of two independent Gaussians ($\sigma_{\text{unbias,corr}} = 25.90\,\text{MeV/c}^2$).

   - The function

   $$\sigma_{IM}(\kappa) = \sigma_{\text{unbias}} + \frac{\sigma_{\text{mis-ID}}}{1 + r \cdot \exp(\kappa/\kappa_0)} + \frac{\sigma_{\text{double mis-ID}}}{(1 + r \cdot \exp(\kappa/\kappa_0))^2}, \quad (6.10)$$

   which takes the contribution of a mis-identification of both particles into account ($\sigma_{\text{unbias,corr}} = 26.47\,\text{MeV/c}^2$). As expected the fit results gives a value compatible with zero ($\sigma_{\text{double mis-ID}} = (1.01 \pm 2.08) \cdot 10^{-4}$).

We add the different systematics uncertainties quadratically and take the square root to gain the total systematic uncertainty. This is done as the major contributions (Binning scheme, GL cut and fit function for $\sigma_{IM}(\kappa)$) are independent from each other. We obtain for the total systematic uncertainty a value of $\pm 1.5\,\text{MeV/c}^2$.

The final result is

$$B^0_{(s)} \to \mu^+ \mu^- : \qquad \boxed{\sigma = 26.5 \pm 0.6\,(\text{stat.}) \pm 1.5\,(\text{syst.})\,\text{MeV/c}^2} \qquad (6.11)$$

**Table 6.2:** Systematic uncertainties on $\sigma_{\text{unbiased,corr}}$ extracted from the inclusive decay mode $B^0_{(s)} \to h^+h^-$

| Systematic uncertainty | Value |
|---|---|
| GL cut | $\pm 0.63$ MeV/c$^2$ |
| Considered range of $\kappa$ | $\pm 0.22$ MeV/c$^2$ |
| Steps in $\kappa$ | $\pm 0.26$ MeV/c$^2$ |
| Correction factor $\gamma$ | $\pm 0.23$ MeV/c$^2$ |
| Binning scheme of the efficiency determination | $\pm 1.09$ MeV/c$^2$ |
| Fit function for the invariant mass distribution | $\pm 0.43$ MeV/c$^2$ |
| Fit function for $\sigma_{IM}(\kappa)$ | $\pm 0.56$ MeV/c$^2$ |
| Total systematic | $\pm 1.51$ MeV/c$^2$ |

which is in very good agreement to the results obtained from the interpolation method which are:

$$B^0 \to \mu^+\mu^- : \qquad \sigma = 27.4 \pm 0.3 \text{ (stat.) } \pm 1.0 \text{ (syst.) MeV/c}^2$$
$$B^0_s \to \mu^+\mu^- : \qquad \sigma = 27.8 \pm 0.3 \text{ (stat.) } \pm 1.1 \text{ (syst.) MeV/c}^2$$

# 7 Determination of the Transition Point $\alpha$ and the Exponent $n$ of the Crystal Ball function

The values of the transition point $\alpha$ and the exponent $n$ of the Crystal Ball function (3.3) are extracted from $B_s^0 \to \mu^+\mu^-$ Monte Carlo. This method is chosen as these parameters are strongly correlated with the width $\sigma$ of the Gaussian part of the Crystal Ball function. Furthermore, the exponent $n$ depends mainly on the spectrum of the final state radiation (FSR) and on the energy loss of the final state particles in the detector material. Both these effects should be well described in the Monte Carlo simulation. The idea for the extraction is that we consider the true mass of $B_s^0$, i.e. the invariant mass unbiased from the detector resolution, but incorporating the effects of FSR and energy loss in the detector components. This true mass is then smeared by a gaussian with a width based on the determined invariant mass resolution determined in the previous two chapters.

## 7.1 Theoretical Consideration

### 7.1.1 Turning Point $\alpha$

The turning point $\alpha$ is the position along the invariant mass axis, measured in units of $\sigma$ away from the peak position, where the Crystal Ball function changes from the Gaussian to the exponential regime defined by the exponent $n$. The coarser the invariant mass resolution is, the more the FSR is buried beneath the smearing of the invariant mass due to its resolution. Therefore a larger invariant mass resolution should lead to a higher value of $\alpha$.

### 7.1.2 Exponent $n$

The exponent $n$ of the Crystal Ball function is linked to the spectrum $\rho(E_\gamma)$ of the FSR by

$$\rho(E_\gamma) \propto E_\gamma^{-n}. \tag{7.1}$$

We expect a spectrum of the FSR which is to first order proportional to the inverse of the photon energy, therefore we expect $n = 1$ [7].

## 7.2 Estimation from Monte Carlo Data

### 7.2.1 Combined values of $\sigma$

To obtain the width for the gaussian smearing we combine the two results for the invariant mass resolution presented in Chapters 5 and 6.
As the two results are in good agreement we take their weighted average. The systematics of the two methods are not correlated with each other. Therefore we take here for the combined statistical as well as for the systematic error the standard combination for weighted averages, i.e.

$$\sigma_{\text{stat./syst.}} = \sqrt{\frac{1}{\sum_i \frac{1}{\sigma_{i,\text{stat./syst.}}}}}, \tag{7.2}$$

where $i$ is the index for the different methods.
The combined results (cf. Fig. 7.1) are:

$$B^0 \to \mu^+\mu^- : \qquad \boxed{\sigma = 27.1 \pm 0.3 \,(\text{stat.}) \,\pm 0.8 \,(\text{syst.}) \,\text{MeV/c}^2} \tag{7.3}$$

$$B_s^0 \to \mu^+\mu^- : \qquad \boxed{\sigma = 27.4 \pm 0.3 \,(\text{stat.}) \,\pm 0.9 \,(\text{syst.}) \,\text{MeV/c}^2} \tag{7.4}$$

The determined value of $\sigma$ depends in principle also on the values for $n$ and $\alpha$ chosen in the analyses in the previous two chapters. We neglect this second order effect by considering only the influence of $\sigma$ on $n$ and $\alpha$ and not vice versa.

### 7.2.2 Determination of $\sigma_{\text{smear}}$

The correct parameter $\sigma_{\text{smear}}$ for the Gaussian smearing does not necessarily have to be the invariant mass resolution in (7.3) and (7.4) as there might be interactions of the final state particles with the material of the detector. To obtain the correct value for $\sigma_{\text{smear}}$ we
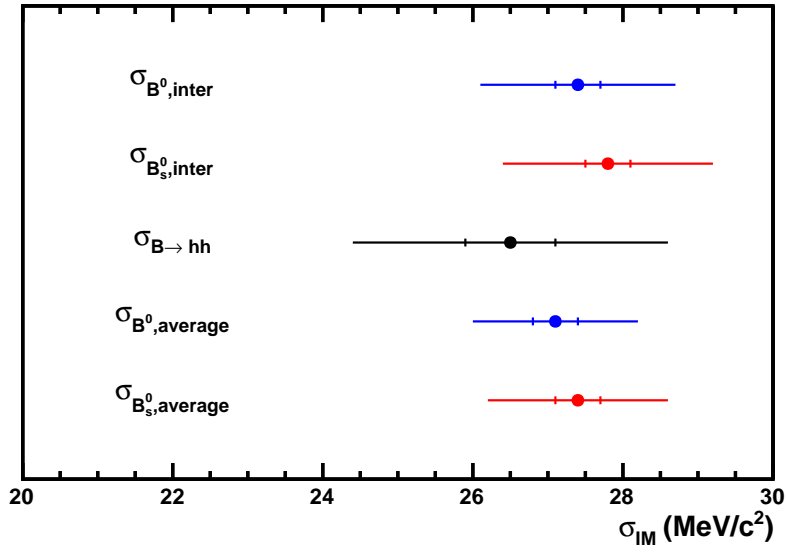
**Figure 7.1:** Summary of the different estimates for the invariant mass resolution $\sigma$ obtained by the interpolation method and the method based on $B^0_{(s)} \to h^+h^-$. The ticks mark the contribution of the statistical error.



**Figure 7.2:** The reconstructed invariant mass resolution $\sigma$, extracted from the fit of the invariant mass distribution, as a function of the value of $\sigma_{\text{smear}}$ used to perform the Gaussian smearing of the true invariant mass. $\sigma_{IM}$ has an about 2% higher value than $\sigma_{\text{smear}}$.

consider the invariant mass distribution of the true mass smeared by $\sigma_{smear}$ for a range of $\sigma_{smear} \in [10, 50]$ MeV/c$^2$. The reconstructed invariant mass resolution is defined as the width $\sigma$ of the single Crystal 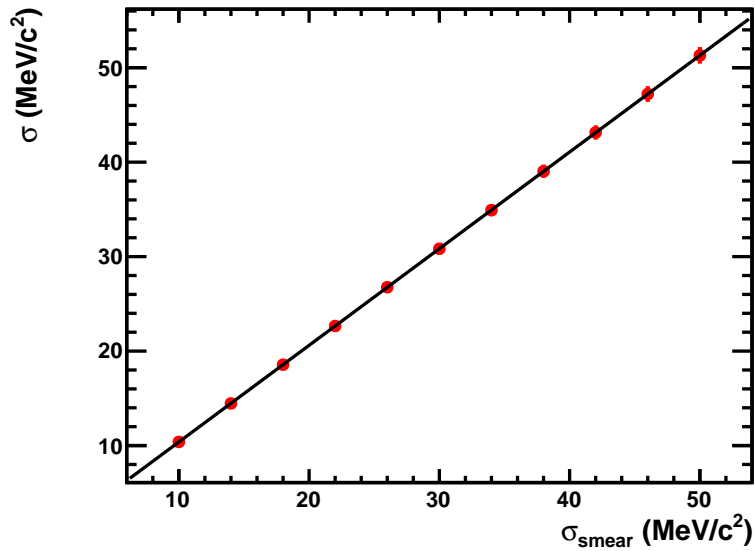Ball function fitted to the smeared invariant mass resolution. For certain value of $\sigma_{smear}$ one thousand smeared invariant mass distributions are produced and the mean of the one thousand resulting values from the fit is taken as value for the reconstructed resolution.

Fig. 7.2 shows the reconstructed resolutions as a function of the smearing parameter $\sigma_{smear}$ which can be well parametrized by a linear function $\sigma = a_0 + a_1 \cdot \sigma_{smear}$ having the parameters $a_0 = (0.15 \pm 0.17)$ MeV/c$^2$ and $a_1 = (1.023 \pm 0.008)$. As expected, $a_1$ is larger than 1 and the correct width for the gaussian smearing is smaller than the invariant mass resolution. We obtain:

$$B^0 \to \mu^+\mu^- : \qquad \sigma_{smear} = 26.3 \pm 0.9 \text{ MeV/c}^2 \qquad (7.5)$$

$$B_s^0 \to \mu^+\mu^- : \qquad \sigma_{smear} = 26.6 \pm 1.0 \text{ MeV/c}^2, \qquad (7.6)$$

where the error is the propagated error of the square root of the quadratic sum of the statistical and systematical error on $\sigma$ and of the errors on $a_0$ and $a_1$.

In a second step we produce 20'000 invariant mass distributions smeared with the determined $\sigma_{smear}$, from each of which we extract the parameters $\alpha$ and $n$ by the fit of a single Crystal Ball function. We determine the final values of $\alpha$ and $n$ as the mean of those extracted parameters. As error on $\alpha$ and $n$ we take the means of the errors returned by the fit. This gives us:

$$B^0 \to \mu^+\mu^- : \qquad \alpha = 2.11 \pm 0.05 \qquad (7.7)$$

$$B_s^0 \to \mu^+\mu^- : \qquad \alpha = 2.12 \pm 0.05 \qquad (7.8)$$

and

$$B^0 \to \mu^+\mu^- : \qquad n = 1.01 \pm 0.08 \qquad (7.9)$$

$$B_s^0 \to \mu^+\mu^- : \qquad n = 1.02 \pm 0.08. \qquad (7.10)$$

The exponent $n$ is – as expected from (7.1) – compatible with $n = 1$.

# 7.3 Systematics and Final Results

We take two potential sources of systematics into account. One is the variation of $n$ and $\alpha$ within the error range of $\sigma_{smear}$. The other is the statistical uncertainty on the extracted parameter due to the random nature of the Gaussian smearing. The systematic uncertainties assigned to these two sources are listed in Tab. 7.1.

1. **Error on $\sigma_{smear}$:** We consider the dependency of each of these two variables on the value of $\sigma_{smear}$ while the other of the two variables is kept constant. The results are shown in Fig. 7.3 ($n$; $\alpha$ constant) and 7.4 ($\alpha$; $n$ constant), respectively. In case of $n$ we fit a parabola to the data points and in case of $\alpha$ a linear function. These functions are then used to propagate the errors from $\sigma_{smear}$ to $\alpha$ and $n$ respectively.

2. **Scatter of gaussian smearing:** The systematics caused by the random process of the Gaussian smearing are defined as the standard deviation of the distribution of $\alpha$ and $n$ from the 20'000 smearing iterations.

As those two systematics are not correlated to each other we combine them by taking the square root of the quadratical sum as the total systematic errors.

**Table 7.1:** Systematic uncertainties in the determination of $\alpha$ and $n$

| Systematic uncertainties | Value $B^0$ | | Value $B_s^0$ | |
|---|---|---|---|---|
| | $\alpha$ | $n$ | $\alpha$ | $n$ |
| Error on $\sigma_{smear}$ | $\pm0.05$ | $\pm0.08$ | $\pm0.05$ | $\pm0.08$ |
| Scatter of Gaussian smearing | $\pm0.01$ | $\pm0.01$ | $\pm0.01$ | $\pm0.01$ |
| Total systematic | $\pm0.05$ | $\pm0.08$ | $\pm0.05$ | $\pm0.08$ |

The final results for $\alpha$ are:

$$B^0 \to \mu^+\mu^- : \quad \boxed{\alpha = 2.11 \pm 0.05 \text{ (stat.) } \pm 0.05 \text{ (syst.)}} \tag{7.11}$$

$$B_s^0 \to \mu^+\mu^- : \quad \boxed{\alpha = 2.12 \pm 0.05 \text{ (stat.) } \pm 0.05 \text{ (syst.)}} \tag{7.12}$$

The final results for $n$ are:

$$B^0 \to \mu^+\mu^- : \quad \boxed{n = 1.02 \pm 0.08 \text{ (stat.) } \pm 0.08 \text{ (syst.)}} \tag{7.13}$$

$$B_s^0 \to \mu^+\mu^- : \quad \boxed{n = 1.01 \pm 0.08 \text{ (stat.) } \pm 0.08 \text{ (syst.)}} \tag{7.14}$$

**Figure 7.3:** $n$ as a function of $\sigma_{\text{smear}}$ with $\alpha$ kept constant to the determined value in case of a Gaussian smearing for $B_s^0$. The shape is parametrized by a parabola.
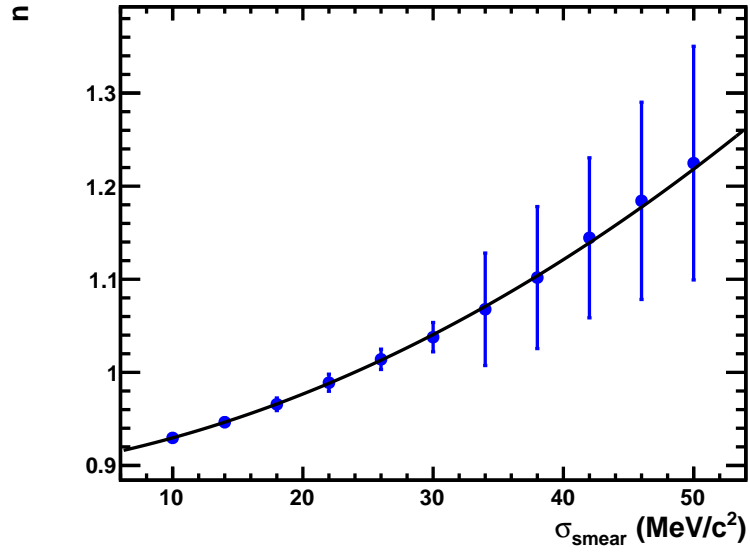


**Figure 7.4:** $\alpha$ as a function of $\sigma_{\text{smear}}$ with $n$ kept constant to the determined value in case of a Gaussian smearing for $B_s^0$. The shape is parametrized by a linear function.

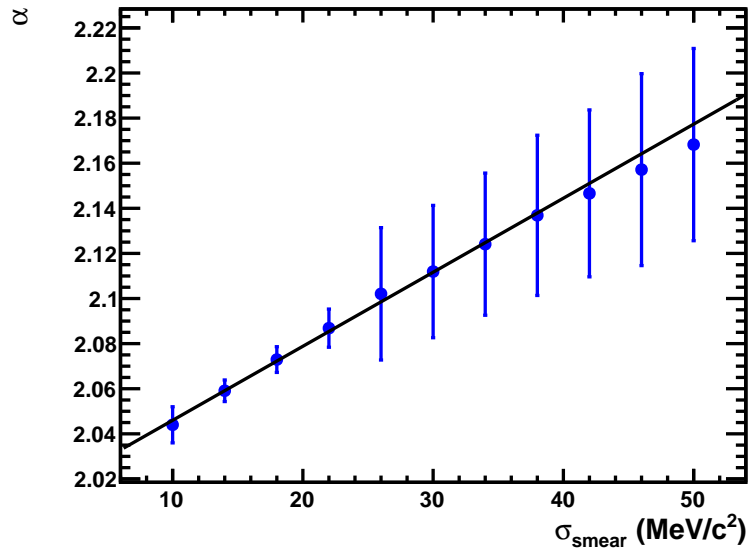# 8 Complete Signal PDF for $B^0_{(s)} \rightarrow \mu^+\mu^-$

The complete signal probability density function (PDF) for $B^0_{(s)} \rightarrow \mu^+\mu^-$ is given by the Crystal Ball function with the parameters estimated in Chapters 4 to 7 and normalized to the mass window of $\pm 60$ MeV/c$^2$ around the nominal $B$ meson masses.

## 8.1 Summary of the Parameters

Tab. 8.1 summarizes the parameters describing the PDF's.

**Table 8.1:** Values, statistical errors and systematic errors for the parameters $\alpha$, $\sigma$, $\mu$ and $n$ for the signal PDF's

| Parameter[a] | $B^0_s \rightarrow \mu^+\mu^-$ | $B^0 \rightarrow \mu^+\mu^-$ |
|---|---|---|
| $\alpha$ | $2.12 \pm 0.05 \pm 0.05$ | $2.11 \pm 0.05 \pm 0.05$ |
| $\sigma$ | $27.4 \pm 0.3 \pm 0.9$ MeV/c$^2$ | $27.1 \pm 0.3 \pm 0.8$ MeV/c$^2$ |
| $\mu$ | $5362.5 \pm 1.6 \pm 2.4$ MeV/c$^2$ | $5275.6 \pm 0.9 \pm 1.5$ MeV/c$^2$ |
| $n$ | $1.01 \pm 0.08 \pm 0.08$ | $1.02 \pm 0.08 \pm 0.08$ |

The correlations among the four parameters are determined from a toy Monte Carlo experiment, using a Gaussian smearing of the true invariant mass from a $B^0_s \rightarrow \mu^+\mu^-$ Monte Carlo sample and fitting a single Crystal Ball function to the resulting distribution. This procedure is repeated 1'000 times to gain the correlation matrix $(\rho)_{ij}$. The results for $B^0_s$ are shown in (8.1), those for $B^0$ in (8.2).

$$\rho = \begin{pmatrix} \rho_{\alpha,\alpha} & \rho_{\alpha,\sigma} & \rho_{\alpha,\mu} & \rho_{\alpha,n} \\ \rho_{\sigma,\alpha} & \rho_{\sigma,\sigma} & \rho_{\sigma,\mu} & \rho_{\sigma,n} \\ \rho_{\mu,\alpha} & \rho_{\mu,\sigma} & \rho_{\mu,\mu} & \rho_{\mu,n} \\ \rho_{n,\alpha} & \rho_{n,\sigma} & \rho_{n,\mu} & \rho_{n,n} \end{pmatrix}$$

$$\rho_{B^0_s} = \begin{pmatrix} 1.00 & 0.2062 & -0.1755 & -0.9202 \\ 0.2062 & 1.00 & -0.1766 & -0.1555 \\ -0.1755 & -0.1766 & 1.00 & 0.1338 \\ -0.9196 & -0.1555 & 0.1338 & 1.00 \end{pmatrix} \qquad (8.1)$$

$$\rho_{B^0} = \begin{pmatrix} 1.00 & 0.2016 & -0.1725 & -0.9196 \\ 0.2016 & 1.00 & -0.1755 & -0.1520 \\ -0.1726 & -0.1755 & 1.00 & 0.1315 \\ -0.9196 & -0.1520 & 0.1315 & 1.00 \end{pmatrix} \tag{8.2}$$

## 8.2 Signal PDF for $B^0_{(s)} \to \mu^+\mu^-$

At the time this thesis is written, the search for $B^0_{(s)} \to \mu^+\mu^-$ has been performed in six equally distributed invariant mass bins in the $\pm 60\,\mathrm{MeV/c^2}$ mass windows around the nominal $B$ meson masses.

The probability that a signal event – inside the mass window – falls into a certain one of these six bins is given by the integral over the bin range of the signal PDF, normalized to the mass window.

The statistical and systematic errors on these probabilities are obtained by a toy Monte Carlo experiment in which the four parameters $\vec{a} = (n, \alpha, \mu, \sigma)$ are randomized by

$$\vec{a}' = \Sigma \cdot \vec{n} + \vec{a}, \tag{8.3}$$

where $\Sigma$ is the Cholesky decomposition of the covariance matrix of these parameters (cf. (8.1), (8.2)) and $\vec{n}$ is a vector containing four normal distributed random numbers.

Fig. 8.1 shows the PDF and the probabilities for the different invariant mass bins for $B^0_s \to \mu^+\mu^-$. The probabilities are summarized in Tab. 8.2. In Fig. 8.2 and Tab. 8.3 the analogue properties are displayed for $B^0 \to \mu^+\mu^-$.
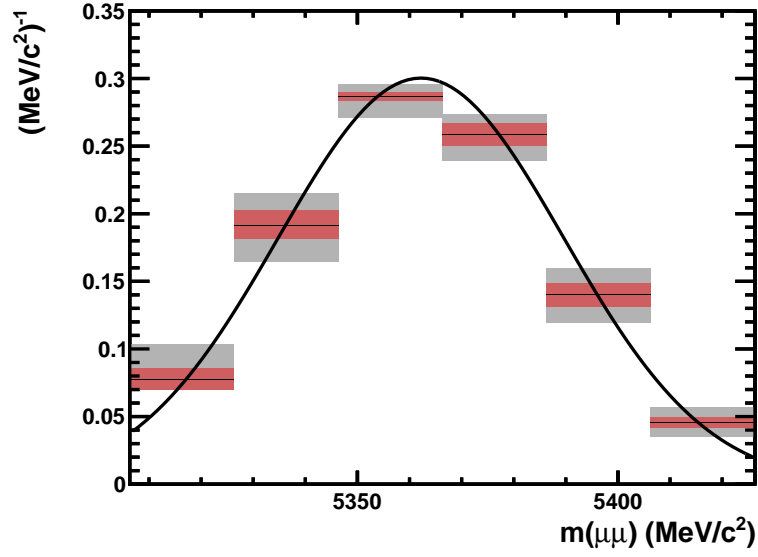
**Figure 8.1:** Signal PDF for $B_s^0 \to \mu^+\mu^-$ described by a Crystal Ball function. The horizontal lines indicate the probability that an event falls into the corresponding invariant mass bin, the red band displays the statistical error, the grey one the systematic error.

**Table 8.2:** Signal distribution in mass bins for $B_s^0 \to \mu^+\mu^-$

| Invariant mass bin | Probability[a] |
|---|---|
| $[5306.3, 5326.3]$ MeV/$c^2$ | $0.078 \pm 0.008^{+0.017}_{-0.001}$ |
| $[5326.3, 5346.3]$ MeV/$c^2$ | $0.191^{+0.011}_{-0.010}{}^{+0.010}_{-0.002}$ |
| $[5346.3, 5366.3]$ MeV/$c^2$ | $0.287 \pm 0.003^{+0.006}_{-0.013}$ |
| $[5366.3, 5386.3]$ MeV/$c^2$ | $0.259^{+0.008}_{-0.009}{}^{+0.006}_{-0.011}$ |
| $[5386.3, 5406.3]$ MeV/$c^2$ | $0.140^{+0.008}_{-0.009} \pm 0.011$ |
| $[5406.3, 5426.3]$ MeV/$c^2$ | $0.046 \pm 0.004^{+0.007}_{-0.006}$ |

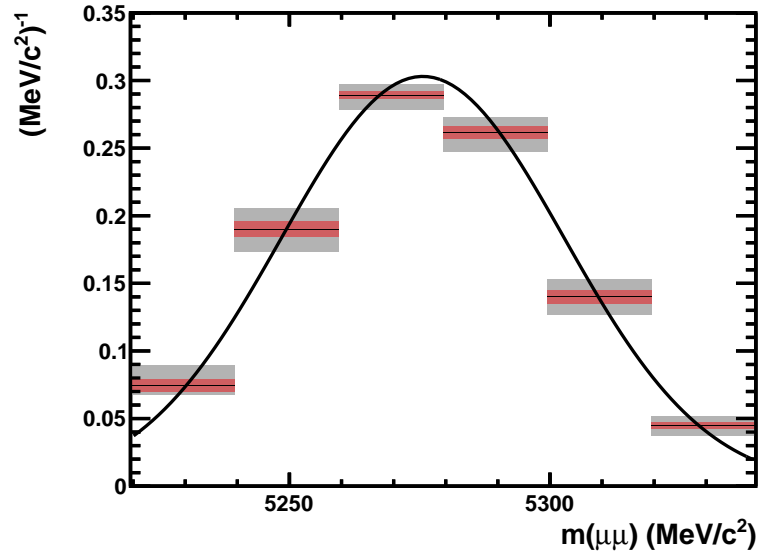[a] The display scheme is 'value', 'statistical error', 'systematic error'

**Figure 8.2:** Signal PDF for $B^0 \to \mu^+\mu^-$ described by a Crystal Ball function. The horizontal lines indicate the probability that an event falls into the corresponding invariant mass bin, the red band displays the statistical error, the grey one the systematic error.

**Table 8.3:** Signal distribution in mass bins for $B^0 \to \mu^+\mu^-$

| Invariant mass bin | Probability[a] |
|---|---|
| [5219.5,5239.5] MeV/c$^2$ | $0.075\pm0.005^{+0.010}_{-0.002}$ |
| [5239.5,5259.5] MeV/c$^2$ | $0.190\pm0.005\pm0.010$ |
| [5259.5,5279.5] MeV/c$^2$ | $0.289\pm0.003^{+0.006}_{-0.007}$ |
| [5279.5,5299.5] MeV/c$^2$ | $0.261\pm0.005^{+0.006}_{-0.009}$ |
| [5299.5,5319.5] MeV/c$^2$ | $0.140\pm0.005^{+0.008}_{-0.009}$ |
| [5319.5,5339.5] MeV/c$^2$ | $0.045\pm0.003\pm0.005$ |

[a] The display scheme is 'value', 'statistical error', 'systematic error'

# Summary

The data in Tab. A and B (same as in Tab. 8.2 and 8.3) provides the distribution of expected signal events in the six invariant mass bins within the mass window for the search of $B^0_{(s)} \to \mu^+\mu^-$. The results are based on a probability density function parametrized by a Crystal Ball function. The parameters of the PDF have been extracted from collision data, using dimuon resonances and decay modes $B^0_{(s)} \to h^+h^-$ with $h \in \{K, \pi\}$ as well as from $B^0_s \to \mu^+\mu^-$ Monte Carlo. Afterwards, the distribution of expected signal events compared to the distribution of measured events is used as an input for the determination of upper limits for the branching fractions $\mathcal{B}(B^0_{(s)} \to \mu^+\mu^-)$ by the binned $CL_s$ method.
The analysis for the data collected by LHC*b* in 2010 was finished in spring 2011 and the published upper limits for the branching fractions are [2]:

$$\mathcal{B}(B^0_s \to \mu^+\mu^-) \quad < 5.6 \cdot 10^{-8} \quad \text{at 95\% C.L.}$$
$$\mathcal{B}(B^0 \to \mu^+\mu^-) \quad < 1.5 \cdot 10^{-8} \quad \text{at 95\% C.L.}$$

**Table A:** Signal distribution in mass bins for $B^0_s \to \mu^+\mu^-$

| Invariant mass bin | Probability[a] |
|---|---|
| [5306.3,5326.3] MeV/c$^2$ | $0.078 \pm 0.008^{+0.017}_{-0.001}$ |
| [5326.3,5346.3] MeV/c$^2$ | $0.191^{+0.011}_{-0.010}{}^{+0.010}_{-0.002}$ |
| [5346.3,5366.3] MeV/c$^2$ | $0.287 \pm 0.003^{+0.006}_{-0.013}$ |
| [5366.3,5386.3] MeV/c$^2$ | $0.259^{+0.008}_{-0.009}{}^{+0.006}_{-0.011}$ |
| [5386.3,5406.3] MeV/c$^2$ | $0.140^{+0.008}_{-0.009} \pm 0.011$ |
| [5406.3,5426.3] MeV/c$^2$ | $0.046 \pm 0.004^{+0.007}_{-0.006}$ |

[a] The display scheme is 'value', 'statistical error', 'systematic error'

**Table B:** Signal distribution in mass bins for $B^0 \to \mu^+\mu^-$

| Invariant mass bin | Probability[a] |
|---|---|
| [5219.5,5239.5] MeV/c$^2$ | $0.075 \pm 0.005^{+0.010}_{-0.002}$ |
| [5239.5,5259.5] MeV/c$^2$ | $0.190 \pm 0.005 \pm 0.010$ |
| [5259.5,5279.5] MeV/c$^2$ | $0.289 \pm 0.003^{+0.006}_{-0.007}$ |
| [5279.5,5299.5] MeV/c$^2$ | $0.261 \pm 0.005^{+0.006}_{-0.009}$ |
| [5299.5,5319.5] MeV/c$^2$ | $0.140 \pm 0.005^{+0.008}_{-0.009}$ |
| [5319.5,5339.5] MeV/c$^2$ | $0.045 \pm 0.003 \pm 0.005$ |

[a] The display scheme is 'value', 'statistical error', 'systematic error'

# Bibliography

[1] R. Aaji et al. [LHC*b* collaboration], *Search for the rare decays $B^0_{(s)} \to \mu^+\mu^-$ with 300 pb$^{-1}$ at LHC*b, LHCb-CONF-2011-037, (2011)

[2] R. Aaji et al. [LHC*b* collaboration], *Search for the rare decays $B^0_{(s)} \to \mu^+\mu^-$*, Phys. Lett. B, 699 (2011), 330

[3] R. Aaji et al. [LHC*b* collaboration], *Measurement of $\sigma(pp \to b\bar{b}X)$ at $\sqrt{s} = 7\,TeV$ in the forward region*, Phys. Lett. B, 694 (2010), 209

[4] T. Aaltonen et al. [CDF Collaboration], *Search for $B^0_s \to \mu^+\mu^-$ and $B^0 \to \mu^+\mu^-$ with CDF II*, arXiv:1107.2304v1 [hep-ph] (2011)

[5] T. Aaltonen et al. [CDF Collaboration], *Search for $B^0_s \to \mu^+\mu^-$ and $B^0_d \to \mu^+\mu^-$ decays in 3.7 fb$^{-1}$ of $p\bar{p}$ collisions with CDF II*, CDF Public Note 9892

[6] V. Abazov et al. [DØ Collaboration], *Search for the rare decay $B^0_s \to \mu^+\mu^-$*, Phys. Lett. B 693 (2010), 539

[7] T. M. Aliev et al., *Rare radiative $B \to \tau^+\tau^-\gamma$ decay*, Phys. Lett. B, 424 (1998), 175

[8] A. A. Alves et al. [LHC*b* collaboration], *The LHC*b *Detector at the LHC*, JINST 3, (2008)

[9] A. A. Alves et J. Magnin, *Measuring asymmetries in avor asymmetric machines*, arXiv:1101.0116v1, (2010)

[10] M. Artuso et al., *B, D and K decays*, arXiv:0801.1833v1 [hep-ph] (2008)

[11] D. Asner et al. [Heavy Flavor Averaging Group], *Averages of b-hadron, c-hadron, and $\tau$-lepton Properties*, arXiv:1101.1589v2 [hep-ph] (2011)

[12] H. Baer et al., *Updated reach of CERN LHC and constraints from relic density, $b \to s\gamma$ and $a_\mu$ in the mSUGRA model*, arXiv:0304303v2 [hep-ph] (2003)

[13] A. Buras et al., *EDMs vs CPV in $B_{s,d}$ mixing in two Higgs doublet models with MFV*, arXiv:1007.5291v2 [hep-ph] (2010)

[14] A. Buras, *Minimal Flavour Violation and beyond: Towards a flavour code for short distance dynamics*, arXiv:1012.1447v2 [hep-ph] (2011)

[15] A. Carbone et al., *Invariant mass line shape of $B \to PP$ decays at LHCb*, LHCb-PUB-2009-031, (2009)

[16] S. Chatrchyan et al. [CMS collaboration], *Search for $B_s^0 \to \mu^+\mu^-$ and $B^0 \to \mu^+\mu^-$ in pp collisions at $\sqrt{s} = 7\,TeV$*, CERN-PH-EP/2011-120, (2011)

[17] G. Lanfranchi et al., *The Muon Identification Procedure of the LHCb Experiment for the First Data* , LHCb-PUB-2009-013, (2009)

[18] J. E. Gaiser, *Charmonium Spectroscopy from Radiative Decays of the J/$\psi$ and $\psi'$*, PhD thesis, SLAC R-255 (1982)

[19] A. Gallas [LHCb collaboration], *Commissioning and Early Physics at LHCb*, Journal of Physics: Conference Series, 171 (2009), 012056

[20] R. L. Gluckstern, *Uncertainties in Track Momentum and Direction, due to Multiple Scattering and Measurement Errors*, Nucl. Instr. Meth., 24 (1963), 381-389

[21] Jose A. Hernando [LHCb collaboration], *Statistical methods used on searches at LHCb, with special emphasis in the search for the very rare decay $B_s \to \mu^+\mu^-$*, Proceedings of PhysStat2011 (17-21 January 2011, CERN), (2011)

[22] K Kleinknecht, *Detectors for Particle Radiation*, 2nd edition, Cambridge University Press, 1998

[23] U. Kerzel [LHCb collaboration], *The LHCb RICH Detectors*, Journal of Physics: Conference Series 110 (2008), 092014

[24] P. Langacker, *The Physics of Heavy Z' Gauge Bosons*, arXiv:0801.1345v3 [hep-ph] (2009)

[25] K. Nakamura et al. [Particle Data Group], *The Review of Particle Physics*, J Phys. G 37, 075021 (2010)

[26] Andrew Powell [LHCb collaboration], *Reconstruction and PID performance of the LHCb RICH detectors*, Nucl. Instr. Meth. A, Vol 639, Issue 1, p. 260-263 (2011)

[27] A. L. Read, *Modified Frequentist Analysis of Search Results (The $CL_s$ Method)*, CERN-OPEN-2000-205 (2000)